



Modelling the three-dimensional, diagnostic fabric anisotropy field of an ice rise

A. Clara J. Henry^{1,2} , Carlos Martín³  and Reinhard Drews² 

¹Max Planck Institute for Meteorology, Hamburg, Germany; ²Department of Geosciences, University of Tübingen, Tübingen, Germany and ³British Antarctic Survey, Natural Environment Research Council, Cambridge, UK

Article

Cite this article: Henry ACJ, Martín C, Drews R (2025) Modelling the three-dimensional, diagnostic fabric anisotropy field of an ice rise. *Journal of Glaciology* **71**, e31, 1–16. <https://doi.org/10.1017/jog.2025.14>

Received: 2 August 2024
Revised: 27 February 2025
Accepted: 27 February 2025

Keywords:

Anisotropic ice; Antarctica; crystal orientation; ice-sheet modelling; ice rise

Corresponding author: A. Clara J. Henry;
Email: clara.henry@math.su.se

A. Clara J. Henry is presently at Department of Mathematics, Stockholm University, Sweden

Abstract

Polar ice develops anisotropic crystal orientation fabrics under deformation, yet ice is mostly modelled as an isotropic fluid. We present three-dimensional simulations of the crystal orientation fabric of Derwael Ice Rise including the surrounding ice shelf using a crystal orientation tensor evolution equation corresponding to a fixed velocity field. We use a semi-Lagrangian numerical method that constrains the degree of crystal orientation evolution to solve the equations in complex flow areas. We perform four simulations based on previous studies, altering the rate of evolution of the crystal fabric anisotropy and its dependence on a combination of the strain rate and deviatoric stress tensors. We provide a framework for comparison with radar observations of the fabric anisotropy, outlining areas where the assumption of one vertical eigenvector may not hold and provide resulting errors in measured eigenvalues. We recognise the areas of high horizontal divergence at the ends of the flow divide as important areas to make comparisons with observations. Here, poorly constrained model parameters result in the largest difference in fabric type. These results are important in the planning of future campaigns for gathering data to constrain model parameters and as a link between observations and computationally efficient, simplified models of anisotropy.

1. Introduction

Ice varies from isotropic to anisotropic, with crystals developing a preferred orientation fabric due to ice flow dynamics. Ice crystals tend to align with the direction of an applied force, and shearing of ice is enhanced along basal planes perpendicular to the applied force (Alley, 1988). The orientation of the basal planes is described by a vector referred to as the *c*-axis. The snow grain orientation is initially isotropic, and anisotropic ice fabric develops at a rate dependent on a variety of physical factors including the temperature, pressure and strain rate of the ice. These dependencies allow the investigation of both the steady-state and transient behaviour of ice through the analysis of observational fabric anisotropy data and ice flow models.

Ice cores have long been used to quantify the direction of ice crystals and the degree of fabric anisotropy with depth (Durand and others, 2009; Montagnat and others, 2014; Weikusat and others, 2017). However, the lack of horizontal spatial information hinders the study of the relationship between ice flow and fabric anisotropy. Apart from ice cores sites, anisotropic information is sparse and relies on geophysical methods such as seismics, both active (Diez and others, 2014; Brisbourne and others, 2019) and passive (Smith and others, 2017; Kufner and others, 2023) or radar (Fujita and others, 2006; Drews and others, 2012; Matsuoka and others, 2012). The main limitation is that, generally, seismic methods only provide depth-averaged fabric anisotropy and radar only provides fabric anisotropy information in the horizontal plane, perpendicular to the direction of wave propagation. Recent advances in phase coherent radar systems and data processing for use in inferring ice fabric anisotropy have resulted in an increase in the acquisition of observational fabric data (Dall, 2010; Young and others, 2021a; 2021b; Ershadi and others, 2022; Jordan and others, 2022). These surveys provide the spatial variability of fabric anisotropy in more extensive areas and aid understanding of the relation between fabric anisotropy and ice flow. Prior to this, the lack of observational data to compare with and constrain models has long hindered the progression of ice fabric modelling.

Although we concentrate only on the coupling of the fabric anisotropy field to the velocity and stress fields in the present study, we note that advances in a full coupling of crystal orientation tensor evolution with viscosity are ongoing with challenges remaining regarding numerical instability (Gerber and others, 2023). Several modelling studies investigating the effects of an anisotropic rheology on ice flow dynamics at ice divides in two dimensions (Martin and others, 2009; Martin and Gudmundsson, 2012; Lilien and others, 2023) and in ice streams (Gerber and others, 2023; Richards and others, 2023) have shown the importance of including fabric anisotropy or viscous anisotropy in ice flow models. In idealised, two-dimensional simulations,

© The Author(s), 2025. Published by Cambridge University Press on behalf of International Glaciological Society. This is an Open Access article, distributed under the terms of the Creative Commons Attribution licence (<http://creativecommons.org/licenses/by/4.0>), which permits unrestricted re-use, distribution and reproduction, provided the original article is properly cited.



Richards and others (2022) investigate the influence of the strain rate and spin on the fabric type. Building on the work of Thorsteinsson and others (2003); Gillet-Chaulet and others (2006) and Pettit and others (2007); Rathmann and others (2021) investigated the coupling between fabric anisotropy and viscosity through enhancement factors which result in greater shearing perpendicular to the predominant c -axis direction in two-dimensional numerical ice-flow simulations. Using a computationally efficient anisotropic flow model with a simplified representation of fabric anisotropy coupled to the viscosity via enhancement factors, McCormack and others (2022) studied the effect of fabric anisotropy in larger-scale three-dimensional models.

The coupling of fabric anisotropy evolution in ice flow models is not without complication due to challenges with numerical stability, the parameter choice within the fabric anisotropy evolution equation and the coupling with viscosity in the flow law. Furthermore, because an isotropic assumption has traditionally been employed in ice sheet models, model parameters have been optimised to fit isotropic rather than anisotropic ice flow dynamics. For these reasons, a thorough investigation of each step in the process of modelling ice fabric anisotropy is needed.

In this paper, we present the first model of the three-dimensional, diagnostic, fabric anisotropy field of an ice rise using the finite element model Elmer/Ice (Gagliardini and others, 2013) across 100 partitions and applied to Derwael Ice Rise (DIR). We investigate the dependence of the fabric anisotropy field on the strain rate and deviatoric stress fields without coupling with the viscosity and without re-crystallisation terms, which allows analysis in the absence of the additional feedback complexity. Our simulations provide novel ice fabric predictions for a number of three-dimensional ice-flow settings including areas of vertical-shear-dominated flank flow, grounding zones and shear zones. We highlight areas where geophysical measurements of ice-fabric types would be most informative to constrain relevant model parameters. Furthermore, the direction of the c -axis across the ice rise is investigated to identify regions where a vertical c -axis assumption is valid in radar measurements of fabric anisotropy, providing a novel method for determining the error in eigenvalues with such an assumption.

1.1. Motivation

Our study is motivated by a lack of progress in large-scale ice-sheet models considering crystal orientation fabric. This is despite observations of strong crystal orientation fabric in polar ice (Alley, 1988), knowledge of how anisotropic polar ice is (Duval and others, 1983) and field evidence of the effect crystal orientation fabric has on ice flow (Gerber and others, 2023). After the introduction of the crystal orientation tensor (Gödert, 2003), the flow-induced crystal orientation fabric evolution can be considered by large-scale ice-sheet models (Gagliardini and others, 2013).

We believe that the main reasons for the lack of progress are (a) the numerical implementation of crystal orientation fabric evolution is challenging (Seddik and others, 2011), (b) the interpretation of model output and comparison with non-comprehensive observations is complex (Jordan and others, 2022) and (c) essential model parameters within the theory are not yet constrained by observations (Ma and others, 2010).

Numerically, the main issue is that numerical dispersion tends to break down the orientation tensor properties. Here, we present a numerically robust, three-dimensional model, discuss a framework to interpret model output for comparison with observations

and highlight areas where observations could better constrain model parameters.

1.2. DIR

Ice rises are an ideal study location for understanding ice-flow processes, because transitions between different flow regimes occur over comparatively short spatial scales. Furthermore, ice rises regulate flow from the Antarctic Ice Sheet towards the open ocean, controlling ice shelf velocities and the continental grounding line position (Favier and Pattyn, 2015; Schannwell and others, 2019; 2020; Henry and others, 2022). Formation, evolution and disintegration of ice rises occur over glacial-interglacial timescales, meaning that remnants of ice properties such as temperature and fabric anisotropy from previous flow regimes may become stored in the slow flowing ice of an ice rise.

Ice rises typically have clear ice divides transitioning into a flank-flow regime on all sides with little to no basal sliding (Matsuoka and others, 2015). The grounding line is typically located a few tens of kilometres away from the divide, and the flow field transitions to the surrounding ice shelves through narrow shear zones with large horizontal shear strain rates. We chose DIR (Fig. 1) in East Antarctica as our study site for two reasons. First, we can rely on a predicted three-dimensional steady-state velocity field developed in a previous study (Henry and others, 2023). This velocity field is based on a transient, thermomechanically coupled full Stokes model with an isotropic rheology. The model was forced with an observationally constrained surface mass balance field, and predictions of the model output were validated with extensive radar observations which are available for this Ice Rise (Koch and others, 2024). Second, previous studies suggest that DIR is likely close to steady state (Callens and others, 2016) possibly with a minor amount of thinning (Drews and others, 2015). This justifies the steady-state assumption applied here. DIR is a marine-based ice rise and has a flow divide in the form of a curved arc extended south-west to north-east. The maximum ice thickness is roughly 630 m, and flow velocities in the flank are typically slower than 10 m a^{-1} .

2. Methods

The simulations use output from Henry and others (2023) as a starting point in which the finite element model Elmer/Ice (Gagliardini and others, 2013) was applied to DIR. Most importantly, we use the predicted three-dimensional, steady-state velocity field to make predictions of the fabric anisotropy resulting from a one-way coupling with the crystal orientation evolution equations detailed below.

2.1. Governing equations

The equations of motion for Stokes flow are written as

$$\nabla \cdot (\boldsymbol{\tau} - P\mathbf{I}) + \rho_i \mathbf{g} = 0, \quad (1)$$

where $\boldsymbol{\tau}$ is the deviatoric stress tensor, P is the pressure, \mathbf{I} is the identity matrix, ρ_i is the ice density and $\mathbf{g} = g\hat{\mathbf{e}}_z$ is the gravitational acceleration. The ice is subject to an incompressibility condition,

$$\nabla \cdot \mathbf{u} = 0, \quad (2)$$

and Glen's flow law,

$$\boldsymbol{\tau} = 2\eta\dot{\boldsymbol{\epsilon}}, \quad (3)$$

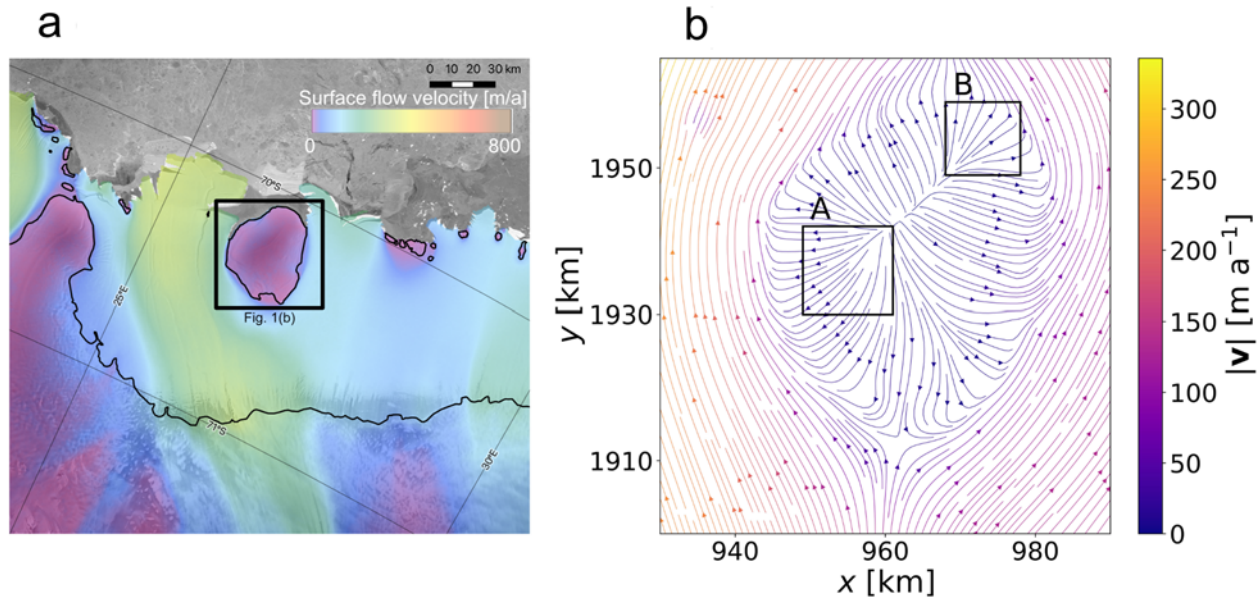


Figure 1. In (a), an overview is shown of DIR, with the surrounding ice shelves and the grounding line (Jezek and others, 2013; Rignot and Scheuchl, 2017). The velocity field is shown in colour. In (b), the simulated upper surface velocity field of DIR is shown, based on simulations in Henry and others (2023). Boxes A and B show the areas referred to as the areas of high horizontal divergence at the tails of the flow divide.

when assuming that ice viscosity is isotropic. This relation describes the nonlinear dependence between the strain rate tensor, $\dot{\epsilon}$, and the deviatoric stress tensor. The effective viscosity, η , is

$$\eta = \frac{1}{2}EA(T')^{-1/n}\dot{\epsilon}_e^{(1-n)/n}, \quad (4)$$

where E is an enhancement factor which is spatially and temporally constant here and $A(T')$ is the ice fluidity which is dependent on the ice temperature relative to the pressure melting point, T' , which is solved using a temperature evolution equation as described in Henry and others (2023). Here, n is Glen’s flow law exponent, and $\dot{\epsilon}_e = \sqrt{\text{tr}\dot{\epsilon}^2}/2$ is the effective strain rate.

When assuming a direction-dependent viscosity, an alternative flow law is defined as

$$\tau = 2\hat{\eta}\dot{\epsilon}, \quad (5)$$

where $\hat{\eta}$ is an anisotropic enhancement tensor. In this study, this equation is calculated using the GOLF model (Castelnau and others, 1996; Gillet-Chaulet and others, 2005; 2006; Gagliardini and others, 2013) although other methods exist (e.g. Rathmann and others (2021)). Such formulations, coupled with an equation describing the evolution of the crystal orientation, can be unstable in fast-flowing areas (Gerber and others, 2023) such as in the ice shelf in the model domain presented here. We therefore use Eq. (3) rather than Eq. (5) as the constitutive law in our model setup. However, a direction-dependent viscosity is used for calculating the crystal orientation evolution, as outlined below.

Keeping the velocity and stress fields constant in time, a semi-Lagrangian fabric anisotropy evolution equation is coupled and simulations are performed for 20000 years. To initialise the fabric anisotropy simulation, the simulation named *n3E0.5dsdt50* in Henry and others (2023) is used. The simulation time of 20000 years was deemed appropriate given that in Henry and others (2023), it was predicted that the ice in DIR is roughly 8000 years old at a depth of 95 %.

The distribution of crystal orientation in a volume of ice can be described by crystal orientation tensors of varying complexity (Advani and Tucker, 1987). Higher-order tensors allow ever-finer details of the crystal orientation distribution to be captured. Such complexity is computationally infeasible, and thus, the description of the crystal orientation tensor is reduced to the second-order crystal orientation tensor, $\mathbf{a}^{(2)}$, and the fourth-order tensor, $\mathbf{a}^{(4)}$, thereby neglecting higher-order tensors (Cintra and Tucker, 1995; Chung and Kwon, 2002). Here, \mathbf{c} is the c -axis unit vector and the operator $\langle \cdot \rangle$ denotes the average over all the grains that compose the ice polycrystal. In reality, $\mathbf{a}^{(2)}$ is dependent on $\mathbf{a}^{(4)}$, which is dependent on $\mathbf{a}^{(6)}$ and so on.

It is useful to compute the eigenvalues and eigenvectors of the second-order crystal orientation tensor, $\mathbf{a}^{(2)}$, in order to understand the fabric anisotropy type. The eigenvalues of $\mathbf{a}^{(2)}$, namely, λ_1, λ_2 and λ_3 , and the corresponding eigenvectors, $\mathbf{v}_1, \mathbf{v}_2$ and \mathbf{v}_3 , of the crystal orientation tensor $\mathbf{a}^{(2)}$ satisfy

$$\mathbf{a}^{(2)}\mathbf{v} = \lambda\mathbf{v}, \quad (6)$$

defining each eigenvalue by its subscript such that $\lambda_1 \leq \lambda_2 \leq \lambda_3$. In the case of randomly oriented c -axes or isotropic ice, all three eigenvalues are similar in size such that $\lambda_1 \approx \lambda_2 \approx \lambda_3 \approx 1/3$. In areas where $\lambda_3 \geq \lambda_1 \approx \lambda_2$, ice fabric is said to have a single maximum fabric with the majority of c -axes pointing in a single direction. Where $\lambda_2 \approx \lambda_3 \geq \lambda_1$, ice is said to have a girdle fabric, with c -axes following an arc or circle. See the Appendix for an explanation of the connection to observational data.

The evolution of the second-order orientation tensor can be described by

$$\left(\frac{\partial}{\partial t} + \mathbf{u} \cdot \nabla\right)\mathbf{a}^{(2)} = \mathbf{W}\mathbf{a}^{(2)} - \mathbf{a}^{(2)}\mathbf{W} - \iota(\mathbf{C}\mathbf{a}^{(2)} + \mathbf{a}^{(2)}\mathbf{C} - 2\mathbf{a}^{(4)} : \mathbf{C}), \quad (7)$$

where the tensor \mathbf{C} is defined by and implemented in our model as

$$\mathbf{C} = (1 - \alpha)\dot{\epsilon} + 2\alpha\hat{\eta}\dot{\epsilon}. \quad (8)$$

Here, α is the so-called interaction parameter, which describes the relative influence of the strain rate and stress tensors, \mathbf{W} is the spin of the ice and $\hat{\boldsymbol{\eta}}$ is the anisotropic enhancement tensor calculated using GOLF (Castelnaud and others, 1996; Gillet-Chaulet and others, 2005; 2006; Gagliardini and others, 2013). The parameter ι determines the rate at which the crystal orientation tensor influenced by the weighted combination of strain rate and deviatoric stress tensors. The last term, $2\alpha \hat{\boldsymbol{\eta}} \dot{\boldsymbol{\epsilon}}$, in Eq. (8) is equivalent to $\alpha k_s A \tau_e^{n-1} \boldsymbol{\tau}$ in Gagliardini and others (2013), so that

$$\mathbf{C} = (1 - \alpha)\dot{\boldsymbol{\epsilon}} + \alpha k_s A \tau_e^{n-1} \boldsymbol{\tau}. \quad (9)$$

We assume that $k_s = 1$, as no given value was published in the studies which we base our parameter choices on (Martin and others, 2009; Seddik and others, 2011; Martin and Gudmundsson, 2012; Gagliardini and others, 2013). Values in other literature have ranged from $k_s < 2.5$ (Gagliardini and Meyssonier, 2002) to $k_s = 10$ (Ma and others, 2010). For each time step, iterations are performed by repeatedly calculating the fabric anisotropy and the direction-dependent viscosity which would result in that fabric anisotropy. This results in a fabric anisotropy which is dependent on a direction-dependent viscosity through the last term in Eq. (8).

Early work recognised the influence of the cumulative strain and stress on ice crystal c -axis orientation (Alley, 1988), which led to the development of a crystal orientation tensor evolution equation (Eq. (7)) dependent on the velocity gradient through the spin and strain rate tensors and the deviatoric stress tensor (Gillet-Chaulet and others, 2006). Although it is known that the velocity and stress fields have an influence on the fabric anisotropy field of ice, it remains unclear what the relative influence is. The fabric anisotropy evolution equation (Eq. (7)) is made up of various terms, with the spin tensor, \mathbf{W} , acting to rotate the crystal orientation tensor to follow the spin of the ice. Acting opposite to the spin tensor is the tensor, \mathbf{C} , which is a weighted combination of the strain rate tensor, $\dot{\boldsymbol{\epsilon}}$, and the deviatoric stress tensor, $\boldsymbol{\tau}$. This combination comes from the fact that the behaviour of macroscopic materials can be limited by two extreme approximations: uniform stress, where the stress in the crystals is assumed to be identical to the macroscopic stress, and Taylor or uniform strain rate, where the strain rate in the crystals is assumed to be identical to the macroscopic strain rate (Gagliardini and others, 2009). The choice of α and ι in previous studies has been motivated by assumptions of the relative influence of stress and strain rate on crystal orientation evolution. The last term in the equation describes the influence of the higher-order crystal orientation tensor, $\mathbf{a}^{(4)}$ on the 3×3 crystal orientation tensor, $\mathbf{a}^{(2)}$.

To solve Eq. (7) we also require a relation between $\mathbf{a}^{(2)}$ and $\mathbf{a}^{(4)}$, a closure approximation, and we use an invariant-based optimal fitting closure approximation (Gillet-Chaulet and others, 2006). The distribution of c -axes can be described by tensors of ever-increasing order, but a compromise is found by using the closure approximation (Advani and Tucker, 1987; Cintra and Tucker, 1995; Chung and Kwon, 2002) in order to reduce computation time. The effect of the choice of α and ι on the fabric anisotropy field is investigated using combinations of parameters from the previous literature presented in Table 1.

The value of α determines the relative influence of the strain rate and deviatoric stress tensors on fabric anisotropy evolution. For example, a value of $\alpha = 0$ means that there is dependence on the strain rate tensor but no dependence on the deviatoric stress. Alternatively, a value of $\alpha = 1$ provides dependence on the deviatoric stress tensor but no dependence on the strain rate tensor.

Table 1. Parameter combinations

	α	ι	Source
(a)	0	1	Martin and others (2009)
(b)	0	0.6	Seddik and others (2011)
(c)	1	1	Martin and Gudmundsson (2012)
(d)	0.06	1	Gagliardini and others (2013)

The parameter ι adjusts the rate at which the fabric anisotropy field develops in response to the weighted combination of the strain rate and deviatoric stress fields and takes a value between $\iota = 0$ and $\iota = 1$.

Initially, all ice in the model domain is isotropic, described by the tensor $\mathbf{a}^{(2)} = \frac{1}{3}\mathbf{I}$, where \mathbf{I} is the 3×3 identity matrix. During transient simulation of the fabric anisotropy field dependent on the velocity field, the upper surface is assigned an isotropic boundary conditions on all ice entering the domain due to accumulation.

The fabric anisotropic evolution model described in Eq. (7) together with its boundary and initial conditions is solved using a semi-Lagrangian method as described in Martin and others (2009). The determinant of $\mathbf{a}^{(2)}$ gives information about the degree of crystal orientation of the fabric (Advani and Tucker, 1987). We define here the degree of crystal orientation with the scalar value,

$$d = 1 - 3^3 \det(\mathbf{a}^{(2)}). \quad (10)$$

The degree of crystal orientation varies from zero for isotropic ice to one for single-maximum fabric and is independent of the frame of reference as the determinant is an invariant. We constrain Equation (7) with the condition,

$$\left(\frac{\partial}{\partial t} + \mathbf{u} \cdot \nabla \right) d \geq 0, \quad (11)$$

meaning that ice is constrained to increase in degree of crystal orientation over time. This constraint on the degree of crystal orientation stops numerical dispersion breaking the simulation in areas with high strain rates. Our method is also straightforward to implement in large-scale models that run in parallel environments.

3. Results

3.1. Analysis of simulated fabric anisotropy field

We display predicted eigenvalues for the $\alpha = 0$, $\iota = 1$ simulation at an elevation of $z = 0$ which encompasses an ice-depth range of close to 0 m in the ice shelf to over 300 m at the ice rise flow divide where stresses are dominated by vertical compression and lateral extension (Fig. 2). The main characteristic, which is evident in all simulations, is that the ice fabric evolves from an isotropic material at the surface and, under deformation, develops into an anisotropic fabric varying from a single maximum to a girdle fabric (Fig. 3). In the ice rise interior, the largest eigenvalue, λ_3 , is much larger than λ_1 and λ_2 , particularly at and surrounding the flow divide (Figs. 1b and 2). This results in greater fabric anisotropy here. Further south in the ice rise, where ice flow is hindered by the convergence of flow between the ice rise and the ice shelf, differences are not as substantial. In the ice rise interior away from the grounding line, differences between the smaller two eigenvalues, λ_1 and λ_2 are mostly small, increasing slightly on the stoss side of the ice rise. The stoss side is defined as the side of the ice rise with a flow direction opposing the upstream ice shelf flow direction (Figs. 1b and 2). At the grounding zone on the stoss side of the ice rise, where horizontal convergence of flow occurs, the three eigenvalues are similar

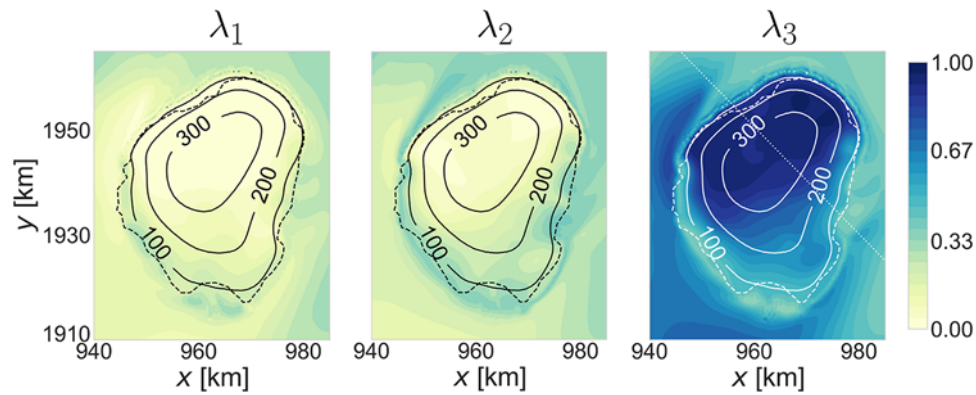


Figure 2. The eigenvalues, λ_1 , λ_2 and λ_3 , of the crystal orientation tensor in the $\alpha = 0$, $\iota = 1$ simulation at an elevation of $z = 0$, corresponding to the sea level. The solid lines, black in the plots showing λ_1 and λ_2 , and white in the plot showing λ_3 , are contours of depth below the upper ice surface, and the dashed lines show the grounding line. The dotted line in the λ_3 figure shows where the cross-section in Figure 3 is taken.

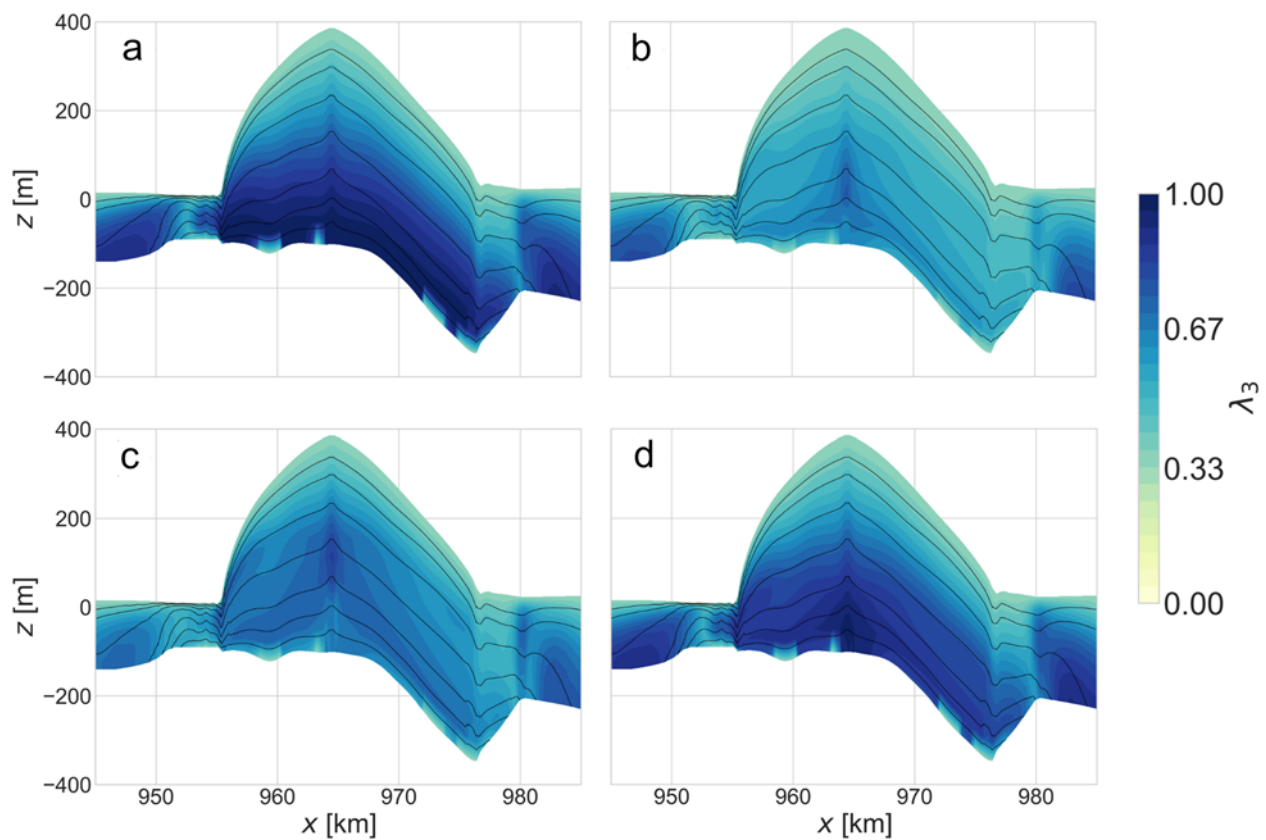


Figure 3. Cross-sections through the flow divide as shown in Figure 2 showing λ_3 , the largest eigenvalue for (a) the $\alpha = 0$, $\iota = 1$ simulation, (b) the $\alpha = 0$, $\iota = 0.6$ simulation, (c) the $\alpha = 1$, $\iota = 1$ simulation and (d) the $\alpha = 0.06$, $\iota = 1$ simulation. The solid lines show isochrones.

in magnitude, whereas at the transition from grounded to floating ice on the lee side of the ice rise, where flow is dominated by extension, a slightly larger difference is seen between the smaller two eigenvalues, λ_1 and λ_2 . In the ice shelves away from the grounding zone, there are differing patterns in the relative magnitude of the three eigenvalues. In the ice shelf west of the ice rise where velocities are higher than east of the ice rise and extension dominates, the largest eigenvalue is significantly larger in magnitude compared with the two smaller eigenvalues. In the ice shelf to the east of the ice rise, where extension of flow is an active process, differences in magnitude are generally much lower. The ice shelf south of the ice

rise, on the stoss side, shows one eigenvalue much larger than the other two, similar to the magnitudes in the ice shelf on the western side of the ice rise.

3.2. Comparison of simulations with differing parameter choice

In order to compare simulation results across the four combinations of the parameters α and ι in Eq. (7) used in the previous studies stated in Table 1, we use a number of metrics to understand the fabric types evolving in the various flow regimes at DIR. First,

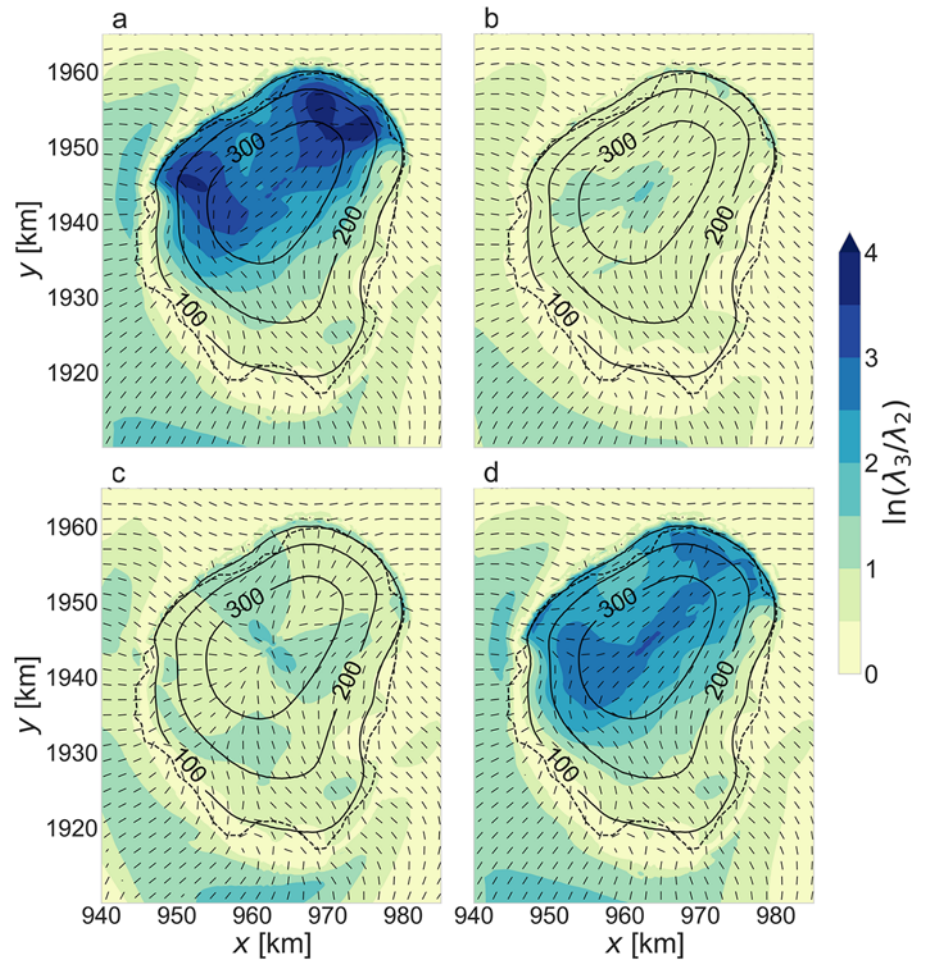


Figure 4. The ratio of the two larger eigenvalues of the 3×3 crystal orientation tensor at $z = 0$ for (a) the $\alpha = 0$, $\iota = 1$ simulation, (b) the $\alpha = 0$, $\iota = 0.6$ simulation, (c) the $\alpha = 1$, $\iota = 1$ simulation and (d) the $\alpha = 0.06$, $\iota = 1$ simulation. The dashes show the maximum horizontal fabric anisotropy direction. The dashed line shows the grounding line, and the solid line shows contours of the depth below the upper ice surface.

we describe the differences in relative magnitude of the eigenvalues of the crystal orientation tensor across the four simulations. If the logarithmic ratio (Woodcock, 1977), $\ln(\lambda_3/\lambda_2)$, is large, then the c -axes are more concentrated in a single direction. The direction of the largest horizontal crystal orientation eigenvector, $\mathbf{v}_{2,H}$, shows the predominant horizontal c -axis direction.

The simulations with parameter choices of $\alpha = 0$, $\iota = 1$ (Fig. 4a) and $\alpha = 0.06$, $\iota = 1$ (Fig. 4d) have comparable results, with a much greater $\ln(\lambda_3/\lambda_2)$ than predicted by the other two simulations. The simulation results differ, however, in the spatial variation of $\ln(\lambda_3/\lambda_2)$. The $\alpha = 0$, $\iota = 1$ simulation shows larger values of $\ln(\lambda_3/\lambda_2)$ at the tails of the ice rise flow divide (Boxes A and B in Figure 1b), whereas the $\alpha = 0.06$, $\iota = 1$ simulation shows slightly greater relative values along the flow divide. Although not negligible, the simulations with parameter choices of $\alpha = 0$, $\iota = 0.6$ (Fig. 4b) and $\alpha = 1$, $\iota = 1$ (Fig. 4c) show much lower ratios between the largest and second largest eigenvalues, with the $\alpha = 0$, $\iota = 0.6$ simulation showing a slightly higher value at the centre of the flow divide. In the $\alpha = 1$, $\iota = 1$ simulation, a differing pattern of horizontal eigenvectors originating at a point source at the flow divide, whereas the other simulations show alignment of the eigenvector direction along the flow divide. Of note is also the differing eigenvector directions at the tails of the flow divide, with differing patterns of vector divergence and convergence.

The two smaller eigenvalues, λ_1 and λ_2 , are investigated using the metric $\ln(\lambda_2/\lambda_1)$ (Fig. 5). Large ratios between the two smaller eigenvalues indicate that c -axis directions for a given volume of ice

are concentrated along an arc. In all simulations, there are high values of $\ln(\lambda_2/\lambda_1)$ at the flow divide and generally low values in the vicinity of the grounding zone on the stoss side of the ice rise, with values differing between simulations elsewhere. The $\alpha = 0$, $\iota = 0.6$ (Fig. 5b) simulation shows the lowest values overall. The simulations with parameter choices of $\alpha = 0$, $\iota = 1$ and $\alpha = 0.06$, $\iota = 1$ show relatively similar results, with the highest eigenvalue ratio at the flow divide and in the areas of the ice rise perpendicular to the flow divide. The $\alpha = 1$, $\iota = 1$ simulation (Fig. 5c) has areas of a large ratio between λ_2 and λ_1 , much larger than any other simulation, and highlights the effect of a strong dependence on the strain-rate tensor on the crystal orientation tensor evolution. Rather than having high values perpendicular to the flow divide, the highest values are along a small band following the flow divide and in the areas of high horizontal divergence at the tails of the flow divide, extending in some areas as far as the grounding line. There are no large differences between λ_2 and λ_1 in the ice shelves, with the largest values being concentrated north-west of the ice rise in all simulations.

The Woodcock k value (Woodcock, 1977), defined as

$$k = \frac{\ln(\lambda_3/\lambda_2)}{\ln(\lambda_2/\lambda_1)}, \quad (12)$$

provides a metric by which to investigate which areas are characterised by a single maximum fabric and which are characterised by girdle fabric. Note that k can have values between $k = 0$ and $k = \infty$. In order to better investigate small values of k , we plot $\ln(k)$ for each simulation in Table 1. If $\ln(k) > 0$, then the ice is defined

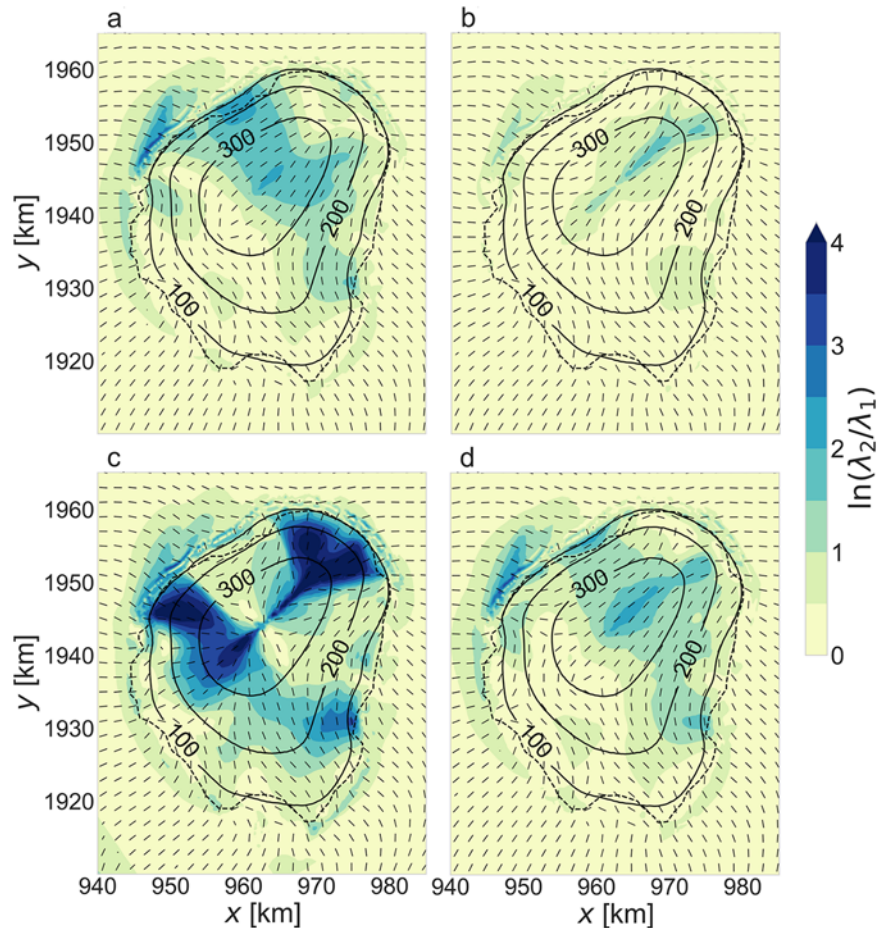


Figure 5. The ratio of the two smaller eigenvalues of the 3×3 crystal orientation tensor at $z=0$ for (a) the $\alpha=0$, $\iota=1$ simulation, (b) the $\alpha=0$, $\iota=0.6$ simulation, (c) the $\alpha=1$, $\iota=1$ simulation and (d) the $\alpha=0.06$, $\iota=1$ simulation. The dashes show the maximum horizontal fabric anisotropy direction. The dashed line shows the grounding line, and the solid line shows contours of the depth below the upper ice surface.

as having a single maximum fabric, and if $\ln(k) < 0$, the ice is defined as having a girdle fabric. Furthermore, if $\ln(k) \gg 0$ and $\ln(\lambda_3/\lambda_2) \gg 0$, then the ice has a strong single maximum. If, on the other hand, $\ln(k) \ll 0$ and $\ln(\lambda_2/\lambda_1) \gg 0$, then ice has a strong girdle fabric.

In the $\alpha=0$, $\iota=1$ simulation, there are relatively high $\ln(k)$ values at the tails of the flow divide (Fig. 6a), extending in some areas almost to the grounding line. Elsewhere on the ice rise, values of $\ln(k)$ are generally close to zero. The $\alpha=0.06$, $\iota=1$ simulation (Fig. 6d) shows similar results except at the north-east of the ice rise, where high values of $\ln(k)$ are concentrated closer to the grounding line. The $\alpha=0$, $\iota=0.6$ simulation (Fig. 6b) shows higher values of $\ln(k)$ even further from the flow divide and a small area with negative $\ln(k)$ values at the north-eastern end of the flow divide. The $\alpha=1$, $\iota=1$ simulation (Fig. 6c) shows, by far, the most negative values of $\ln(k)$, concentrated at the two tails of the flow divide and small areas with positive values of $\ln(k)$ perpendicular to the flow divide. All four simulations show an almost-continuous band of negative values of $\ln(k)$ at the grounding line or a small distance away from the grounding line in the ice shelf. Moving away from the grounding line, a general increase in values of $\ln(k)$ is seen, with some exceptions.

3.3. Metrics for comparison with radar data

In quad-polarimetric radar processing, it is often assumed that because of the dominance of vertical compression, one eigenvector aligns with the vertical direction. In areas where this assumption

holds, signal processing can be simplified (Ershadi and others, 2022; Jordan and others, 2022). Obliquely oriented fabric types can, in theory, also be detected (Matsuoka and others, 2009; Rathmann and others, 2022), but thus far this has not been done for observations which are typically only collected in a nadir-viewing geometry. Here, we present results evaluating the applicability of the assumption of one vertical eigenvector across all four simulations.

In general, the predicted tilt angle is small in the grounded area across all simulations (Fig. 7). Note that the grounded area is the area within the dashed line marking the grounding line. The angle remains small, with similar spatial patterns in the simulations with parameter choices of $\alpha=0$, $\iota=1$ and $\alpha=0.06$, $\iota=1$ (Fig. 7a and d, respectively). In the $\alpha=0$, $\iota=0.6$ simulation (Fig. 7b), differences between the z -direction and v_3 are generally small, with the exception of slightly higher values on either side of the flow divide. Spatial patterns on the stoss side of the ice rise are similar to those in the above-mentioned $\alpha=0$, $\iota=1$ and $\alpha=0.06$, $\iota=1$ simulations. The simulation with the largest tilt angles is the $\alpha=1$, $\iota=1$ simulation (Fig. 7c), with differences of $\pi/8$ to $\pi/4$ radians at and perpendicular to the flow divide. In all simulations, the tilt angle in the ice shelf is larger a short distance away from the grounding line, except for small, isolated areas.

We furthermore calculate the eigenvectors and eigenvalues of the horizontal crystal orientation tensor, i.e. the upper left 2×2 part of the 3×3 tensor $\mathbf{a}^{(2)}$. The reason for this is that if the 3×3 crystal orientation tensor has one strictly vertical eigenvector, the eigenvalues and eigenvectors of the 2×2 tensor correspond to the horizontal eigenvalues and eigenvectors of the 3×3 tensor. We

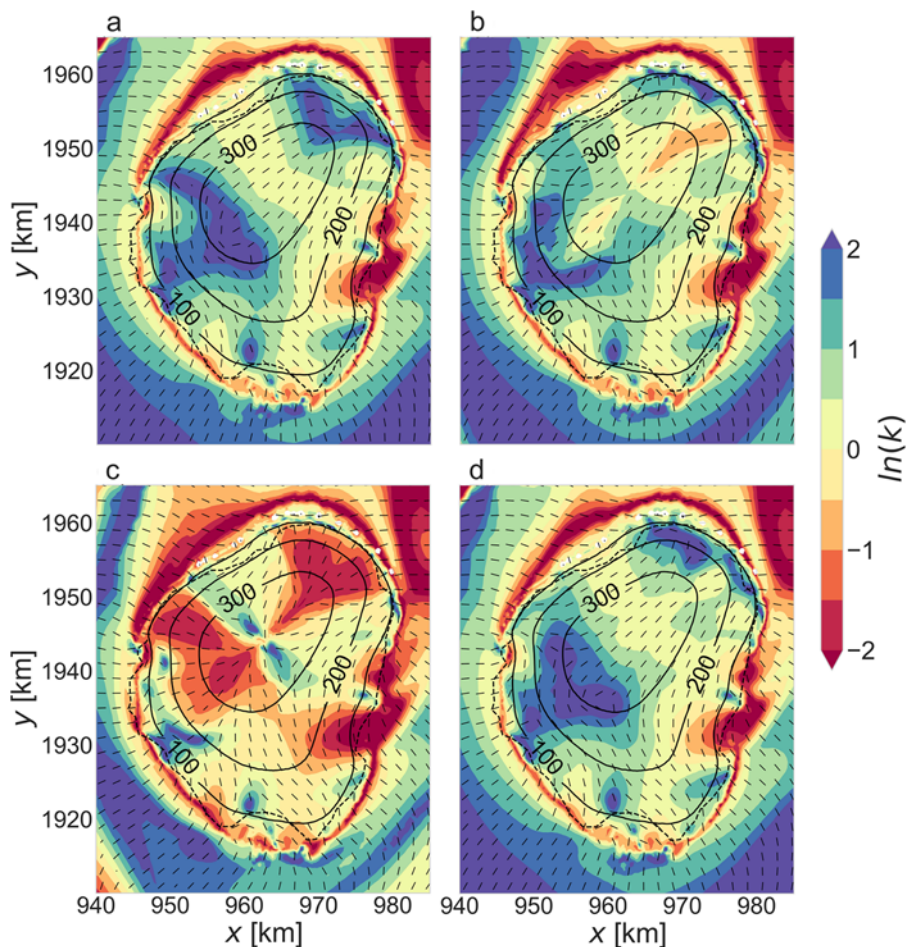


Figure 6. The logarithm of the Woodcock k value at an elevation of $z=0$ for (a) the $\alpha=0, \iota=1$ simulation, (b) the $\alpha=0, \iota=0.6$ simulation, (c) the $\alpha=1, \iota=1$ simulation and (d) the $\alpha=0.06, \iota=1$ simulation. The dashes show the maximum horizontal fabric anisotropy direction. The dashed line shows the grounding line, and the solid line shows contours of the depth below the upper ice surface.

denote the eigenvalues of the 2×2 tensor by $\lambda_{1,H}$ and $\lambda_{2,H}$, and the corresponding eigenvectors by $\mathbf{v}_{1,H}$ and $\mathbf{v}_{2,H}$, respectively. By comparing the eigenvalues of the 2×2 , horizontal crystal orientation tensor with the eigenvalues of the 3×3 crystal orientation tensor, an error estimate can be found for assuming that the eigenvector corresponding to the largest eigenvalue is aligned with the z -axis.

We present percentage differences between λ_1 and $\lambda_{1,H}$ (Fig. 8), as well as λ_2 and $\lambda_{2,H}$ (Fig. 9). We find that if a difference exists between λ_1 and $\lambda_{1,H}$, or λ_2 and $\lambda_{2,H}$, then the 2×2 tensor eigenvalues always underestimate the smaller two 3×3 tensor eigenvalues. Furthermore, percentage differences tend to be higher for the smaller eigenvalues λ_1 and $\lambda_{1,H}$ than for λ_2 and $\lambda_{2,H}$, but exceptions to this are seen. The $\alpha=0, \iota=1$ simulation shows a negligible percentage difference between λ_1 and $\lambda_{1,H}$ (Fig. 8a) and small percentage differences for λ_2 and $\lambda_{2,H}$ of up to 10% (Fig. 9a). A similar spatial distribution of percentage differences appears for λ_2 and $\lambda_{2,H}$ in the $\alpha=0.06, \iota=1$ simulation (Fig. 9d). Most notable is the percentage difference between λ_1 and $\lambda_{1,H}$ in the $\alpha=1, \iota=1$ simulation (Fig. 8c), where values are above 20% in a large area at and perpendicular to the flow divide. In this simulation ($\alpha=1, \iota=1$), percentage differences between λ_2 and $\lambda_{2,H}$ (Figs. 9c) are high compared to other simulations, but the high values localised at and in the area perpendicular to the flow divide occupy a smaller area than the percentage differences between λ_1 and $\lambda_{1,H}$ (Fig. 8c). In the $\alpha=0, \iota=0.6$ and the $\alpha=0.06, \iota=1$ simulations, percentage differences between λ_1 and $\lambda_{1,H}$ are negligible

across a large portion of the ice rise, in particular on the stoss side (Fig. 8b, d). The highest percentage differences are either side of the flow divide with values up to and over 20%, reducing further away from the flow divide. Percentage differences between λ_2 and $\lambda_{2,H}$ in the $\alpha=0, \iota=0.6$ simulation are negligible except for small areas at the flow divide (Fig. 9b). As the assumption that the eigenvector corresponding with the largest eigenvalue is made for grounded ice, we do not analyse the differences between eigenvalues of the 2×2 and the 3×3 crystal orientation tensors in the ice shelves.

Next, we present results for the difference between the eigenvalues, $\lambda_{2,H} - \lambda_{1,H}$, of the 2×2 horizontal part of the 3×3 crystal orientation tensor. This metric corresponds directly with results from radar data where a vertical eigenvector assumption is made (Fig. 10). The $\alpha=0, \iota=1$ (Fig. 10a) and the $\alpha=0.06, \iota=1$ (Fig. 10d) simulations show similar results both spatially and in terms of the magnitude of differences, with differences staying below 0.1 at and in the vicinity of the flow divide. The largest differences in the eigenvalues occur on the eastern side of the ice rise, close to the grounding line as well as in small isolated areas elsewhere on the stoss side of the ice rise in the vicinity of the grounding line. Although eigenvalue differences differ substantially in magnitude between the two simulations, the $\alpha=0, \iota=0.6$ (Fig. 10b) and the $\alpha=1, \iota=1$ (Fig. 10c) simulations show similar spatial patterns. In the $\alpha=0, \iota=0.6$ simulation (Fig. 10b), the highest differences between $\lambda_{2,H}$ and $\lambda_{1,H}$ area seen at the tails of the flow divide, extending towards the grounding line north-east of the ice rise and in isolated areas on the east of the ice

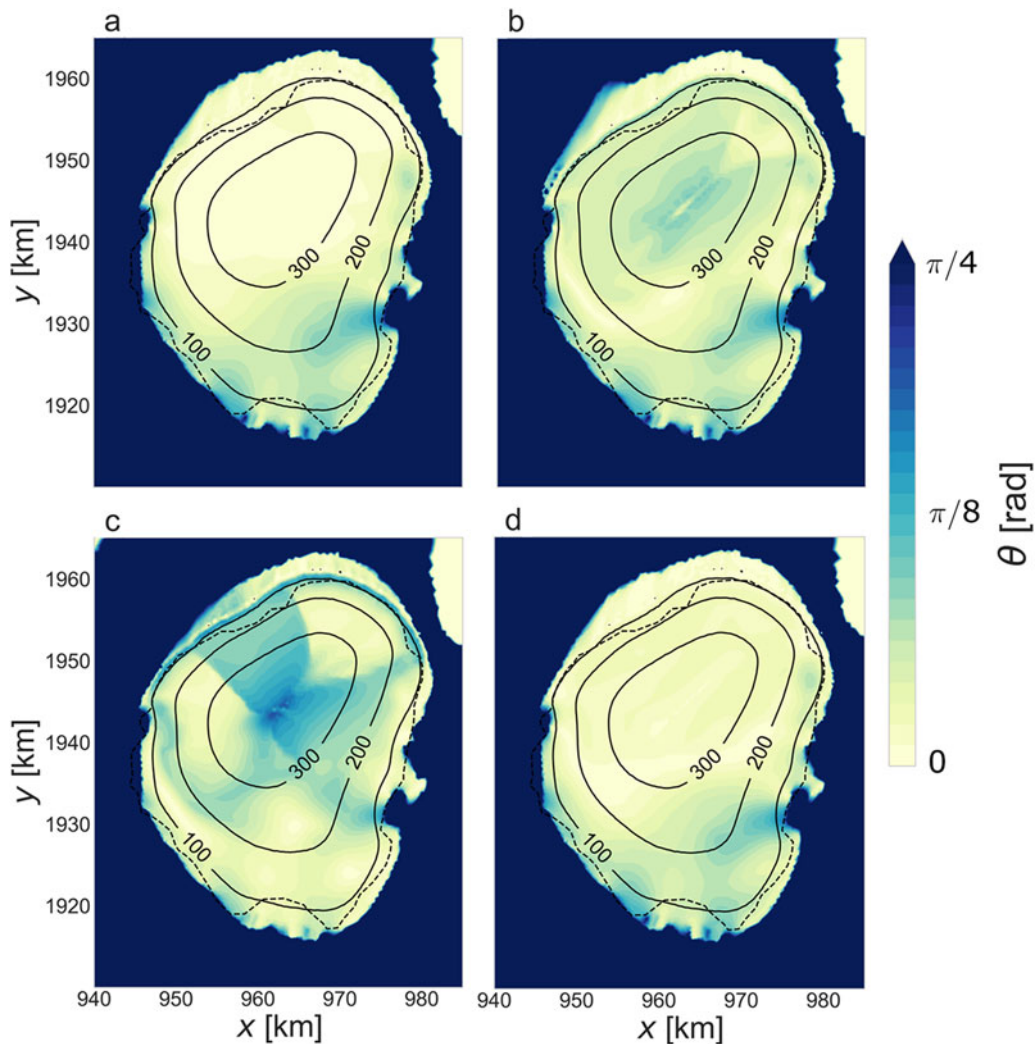


Figure 7. The angle between the eigenvector corresponding to the largest eigenvalue and the vertical direction at an elevation of $z=0$ corresponding to the sea level for (a) the $\alpha=0$, $\iota=1$ simulation, (b) the $\alpha=0$, $\iota=0.6$ simulation, (c) the $\alpha=1$, $\iota=1$ simulation and (d) the $\alpha=0.06$, $\iota=1$ simulation. The dashed line shows the grounding line, and the solid lines show contours for the depth below the surface in metres.

rise. Elsewhere, differences between $\lambda_{2,H}$ and $\lambda_{1,H}$ remain below 0.1. The $\alpha=1$, $\iota=1$ simulation (Fig. 10c) shows large differences between $\lambda_{2,H}$ and $\lambda_{1,H}$ of over 0.3 at the flow divide and extending to the grounding line, particularly on the lee side of the ice rise. As in all other simulations, differences of over 0.3 are seen on the eastern side of the ice rise close to the grounding line.

Finally, we investigate the dependence of the fabric anisotropy field on the strain rate field and, in particular, the relationship between the largest horizontal fabric anisotropy direction and the largest horizontal strain rate direction. Given that we expect c -axes to point perpendicular to the direction of maximum stretching, we calculate the largest horizontal strain rate direction by calculating the eigenvalues and eigenvectors of the upper left 2×2 tensor of the 3×3 strain rate tensor, $\dot{\epsilon}$. We denote the eigenvectors of the horizontal strain rate tensor by $\mathbf{w}_{1,H}$ and $\mathbf{w}_{2,H}$, where $\mathbf{w}_{1,H} \perp \mathbf{w}_{2,H}$. We then calculate the angle between the maximum horizontal strain rate direction, $\mathbf{w}_{2,H}$, and the maximum horizontal fabric anisotropy direction, $\mathbf{v}_{2,H}$ (Fig. 11). In the $\alpha=0$, $\iota=1$ simulation (Fig. 11a) and the $\alpha=0.06$, $\iota=1$ simulation (Fig. 11d), the angle between $\mathbf{w}_{2,H}$ and $\mathbf{v}_{2,H}$ remains close to $\pi/2$, meaning that the two vectors are mostly close to perpendicular. Exceptions

are in small areas of divergence at the two tails of the flow divide. In the $\alpha=0$, $\iota=0.6$ simulation (Fig. 11b), the angle between $\mathbf{w}_{2,H}$ and $\mathbf{v}_{2,H}$ is mainly high everywhere on the ice rise except at the two tails of the flow divide where values are consistently closer to zero. Lastly, the $\alpha=1$, $\iota=1$ simulation (Fig. 11c) shows a large area on the stoss side of the ice rise, away from the flow divide, where $\mathbf{w}_{2,H}$ and $\mathbf{v}_{2,H}$ are mostly close to perpendicular. At the flow divide, there is a thin line where the two vectors are perpendicular and in the areas perpendicular to the flow divide, the angle between the two vectors is generally $> \pi/4$. This simulation shows the largest areas where the angle between $\mathbf{w}_{2,H}$ and $\mathbf{v}_{2,H}$ is close to zero from the extremes of the flow divide as far or almost as far as the grounding line.

4. Discussion

We present the results of three-dimensional simulations of the full-tensor fabric anisotropy field of DIR via a coupling with the velocity and stress fields. The simulated domain includes the surrounding ice shelf, allowing analysis of the fabric anisotropy field across the grounding zone. Based on four previous studies

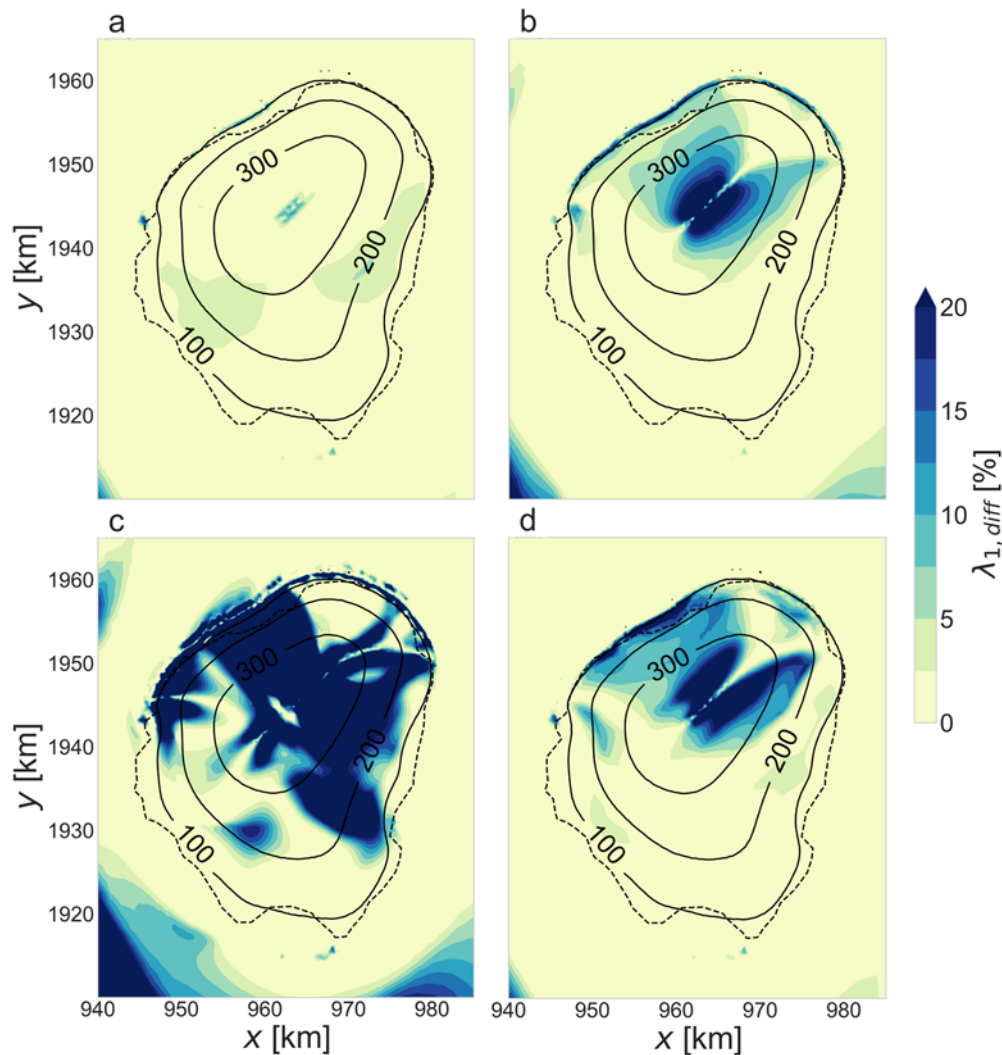


Figure 8. The percentage difference between $\lambda_{1,H}$ and λ_1 at an elevation of $z=0$ for (a) the $\alpha=0, \iota=1$ simulation, (b) the $\alpha=0, \iota=0.6$ simulation, (c) the $\alpha=1, \iota=1$ simulation and (d) the $\alpha=0.06, \iota=1$ simulation. The solid line contours show depth below surface, and the dashed line is the grounding line.

(Martin and others, 2009; Seddik and others, 2011; Martin and Gudmundsson, 2012; Gagliardini and others, 2013), we simulate the fabric anisotropy field varying parameter choices controlling the relative influence of the strain rate and deviatoric stress tensors. By decomposition of the simulated crystal orientation tensor into eigenvalues and eigenvectors, our results provide a necessary step towards the comparison of observed ice fabric with three-dimensional modelled results for a variety of flow regimes.

4.1. Dependence of the fabric anisotropy field on the velocity and stress fields

The various flow regimes in the ice rise influence the fabric anisotropy field in different ways, with past flow regimes of a volume of ice also having an effect on the present fabric anisotropy, which is captured due to the semi-Lagrangian implementation of the crystal orientation tensor evolution in the simulations in this study.

Based on previous choices (Martin and others, 2009; Seddik and others, 2011; Martin and Gudmundsson, 2012; Gagliardini and others, 2013), we adjust the parameters α and ι in Eq. (7). The

parameter α , taking values $\alpha \in [0, 1]$, controls the relative influence of the strain rate and deviatoric stress tensors, with a value of $\alpha=0$ meaning that the deviatoric stress tensor is ignored and a value of $\alpha=1$ meaning that the strain rate tensor is ignored. The parameter ι , taking values of $\iota \in [0, 1]$, controls the rate of change the crystal orientation tensor, $\mathbf{a}^{(2)}$, undergoes in response to the combination of the strain rate and deviatoric stress tensor. For example, for a value of ι close to zero, apart from rotational changes due to the spin tensor, the crystal orientation tensor changes minimally in response to the combination of the strain rate and deviatoric stress tensors. Because the strain rate and deviatoric stress tensor are co-dependent, differentiation between the effect of the various combinations of α and ι on the crystal orientation tensor is not trivial. Broadly speaking, although this is not always the case, the behaviour of the fabric anisotropy field in the $\alpha=0, \iota=0.6$ simulation shows similar results to the $\alpha=1, \iota=1$ simulation, despite the relatively large differences in parameter choice. Conversely, the $\alpha=0, \iota=1$ and the $\alpha=0.06, \iota=1$ simulations show only slightly differing results, likely explained by the similarity in values of α and ι .

While certain anisotropic fabric types can be expected under particular flow and stress regimes, the length of time the ice has

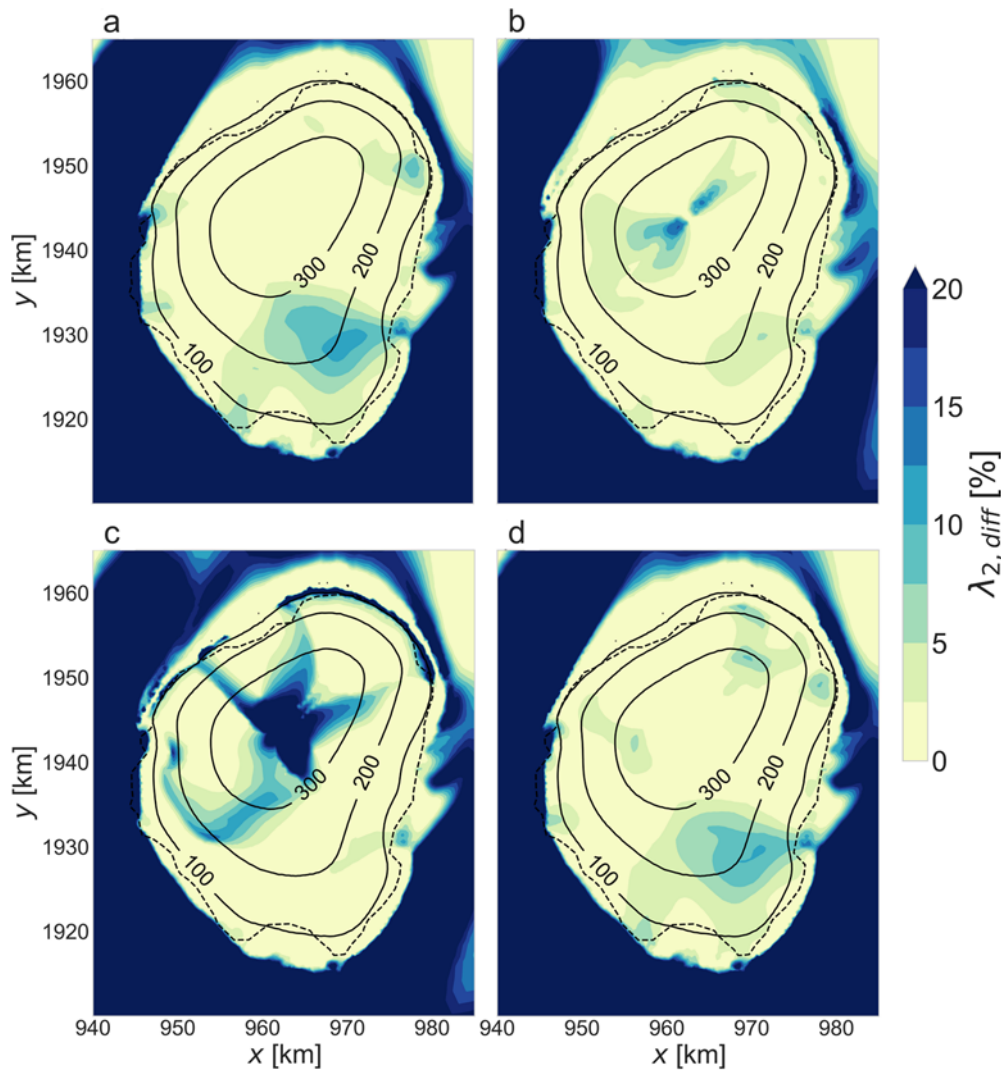


Figure 9. The percentage difference between $\lambda_{2,H}$ and λ_2 at an elevation of $z=0$ for (a) the $\alpha=0, \iota=1$ simulation, (b) the $\alpha=0, \iota=0.6$ simulation, (c) the $\alpha=1, \iota=1$ simulation and (d) the $\alpha=0.06, \iota=1$ simulation. The solid line contours show depth below surface, and the dashed line is the grounding line.

undergone deformation in this regime also has an influence on the reflected fabric anisotropy field. In [Figure 4](#), it can be seen that at the elevation $z=0$, the ice has developed into a relatively strong single maximum fabric in the $\alpha=0, \iota=1$ simulation ([Fig. 4a](#)) and the $\alpha=0.06, \iota=1$ simulation ([Fig. 4d](#)) compared with the other two simulations. On the other hand, the $\alpha=1, \iota=1$ simulation ([Fig. 4c](#)) does not show a strong single maximum. This indicates that the strain rate term of [Eq. \(9\)](#) has a stronger influence on the development of a single maximum under vertical compression at a flow divide than the deviatoric stress tensor term of [Eq. \(9\)](#). Interestingly, in the $\alpha=0, \iota=1$ simulation ([Fig. 4a](#)) and the $\alpha=0.06, \iota=1$ simulation ([Fig. 4d](#)), the areas with a higher single maximum are located at the two tails of the flow divide. Although not explicitly simulated in this study, we expect that the fabric type in the area of high horizontal divergence at the tails of the flow divide would show a similar fabric to that forming at a dome flow divide, defined by a flow divide with horizontal flowlines originating at a point source. In the vicinity of the flow divide, the $\alpha=1, \iota=1$ simulation shows a vastly different horizontal fabric anisotropy direction than the other simulations ([Fig. 5c](#)).

The eigenvector corresponding to the largest horizontal eigenvalue originates at a point source as opposed to being parallel to the flow divide in the other simulations. Values of $\ln(\lambda_2/\lambda_1)$ are high along the flow divide and in relatively large areas where there is high horizontal divergence at the tails of the flow divide, meaning that the ice has a girdle fabric. Of note is that [Figure 11c](#) shows that in the areas of girdle fabric, the maximum horizontal strain rate direction is not perpendicular to the maximum horizontal fabric anisotropy direction. The reason for the differences between the $\alpha=1, \iota=1$ and the other three simulations is due to the largely different α value, which in this case results in ignoring the strain rate tensor completely.

Moving into the flanks of the ice rise, where vertical shear dominates, although the flow of ice in the grounded areas is horizontally divergent, the fabric types vary substantially. We identify a number of factors as having an influence on the ice fabric type: (a) whether flank flow is perpendicular to the flow divide or at the tails of the flow divide, (b) whether the ice is on the stoss or lee side of the ice rise and (c) how close ice is to the grounding line and what type of flow regime is active at the grounding zone. In

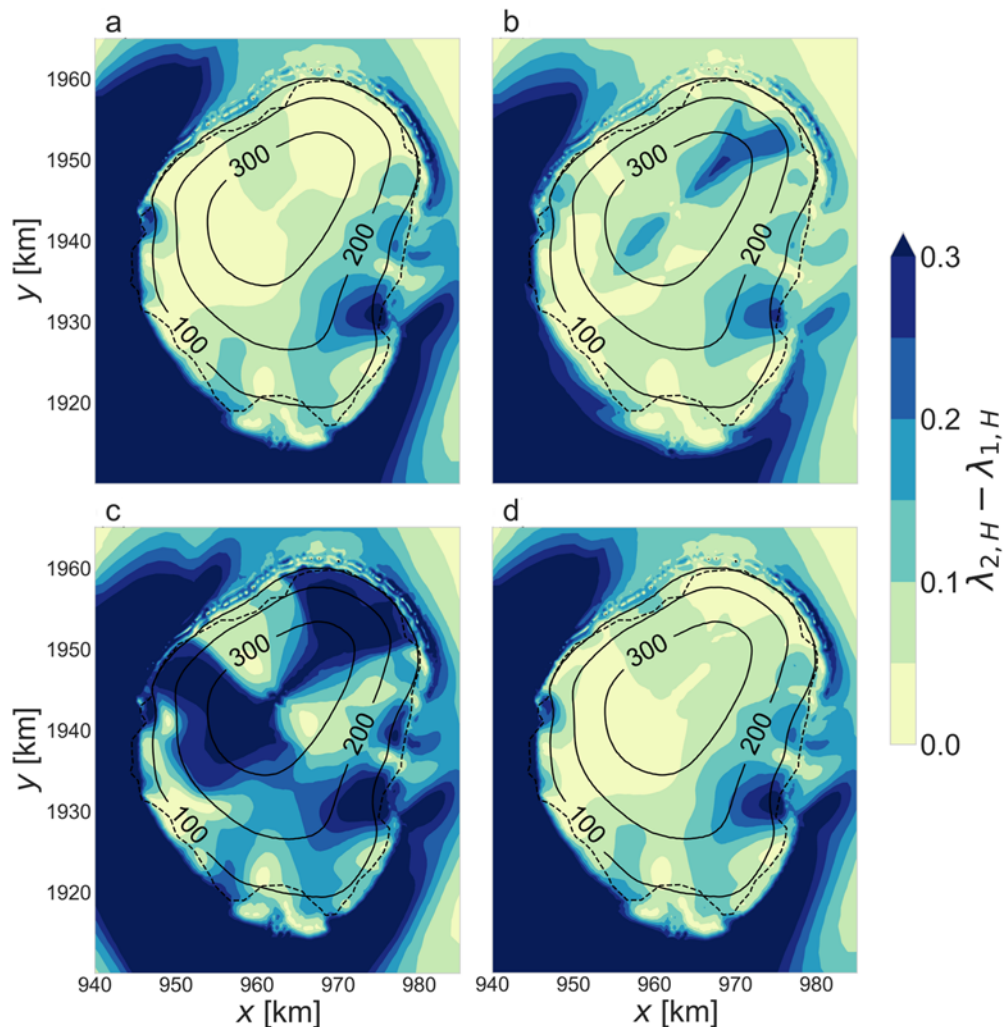


Figure 10. The difference between the two eigenvalues of the 2×2 horizontal crystal orientation tensor for (a) the $\alpha=0$, $\iota=1$ simulation, (b) the $\alpha=0$, $\iota=0.6$ simulation, (c) the $\alpha=1$, $\iota=1$ simulation and (d) the $\alpha=0.06$, $\iota=1$ simulation. The solid lines show contours for the depth below the surface in metres, and the dashed line is the grounding line.

flow regimes dominated by vertical shear, as is the case in the areas perpendicular to the flow divide, it is expected that fabric shows a single maximum with a slight offset to the vertical (Llorens and others, 2022). However, the $\alpha=0$, $\iota=1$ (Fig. 4a) and the $\alpha=0.06$, $\iota=1$ (Fig. 4d) simulations show the strongest single maxima perpendicular to the flow divide, but Figure 7a and d show that these simulations have the smallest tilt angle compared to the other simulations.

Across the grounding line, the predicted $\ln(k)$ values allow differentiation between single maximum fabric ($\ln(k) > 0$) and girdle fabrics ($\ln(k) < 0$, Fig. 6). It must be noted, however, that a large positive or negative value of $\ln(k)$ does not necessarily imply that the ice has a strong single maximum or strong girdle fabric, respectively. Any analysis of the $\ln(k)$ field must be done in conjunction with plots of $\ln(\lambda_2/\lambda_1)$ (Fig. 5) and $\ln(\lambda_3/\lambda_2)$ (Fig. 4) (Woodcock, 1977). In all simulations, ($\ln(\lambda_3/\lambda_2)$) is the lowest at the grounding zone and in the northern and eastern sides of the ice shelf, meaning that there is no single maximum in these areas. Contrary to this, the metric for a girdle fabric ($\ln(\lambda_2/\lambda_1)$) shows a small band at the grounding zone with values of $\ln(\lambda_2/\lambda_1) = 0.5$ to 1. This weak girdle fabric may be due to the transition from a fabric

with a vertical single maximum, to a single maximum aligned with the horizontal plane, via a transition across the grounding zone.

4.2. Implications for viscosity coupling

One ultimate goal in modelling the fabric anisotropy field of ice is to be able to fully couple the velocity and stress fields to the fabric anisotropy field and *vice versa* (note, we will refer to these simulations as *fully coupled* hereafter). In this study, we have explored the influence of the velocity and stress fields on the fabric anisotropy field using three-dimensional simulations, but have not investigated the coupling of the fabric anisotropy field to the velocity field via a direction-dependent viscosity. Here, we discuss areas of DIR where we expect the fabric type to influence viscosity as well as barriers to fully coupled, three-dimensional anisotropic simulations.

Generally speaking, ice crystal *c*-axes rotate in a direction which allows for optimal shearing, with studies showing that if ice is highly anisotropic, deformation in the plane perpendicular to the *c*-axis is significantly enhanced compared with deformation in other directions (Duval and others, 1983). Areas where ice has a

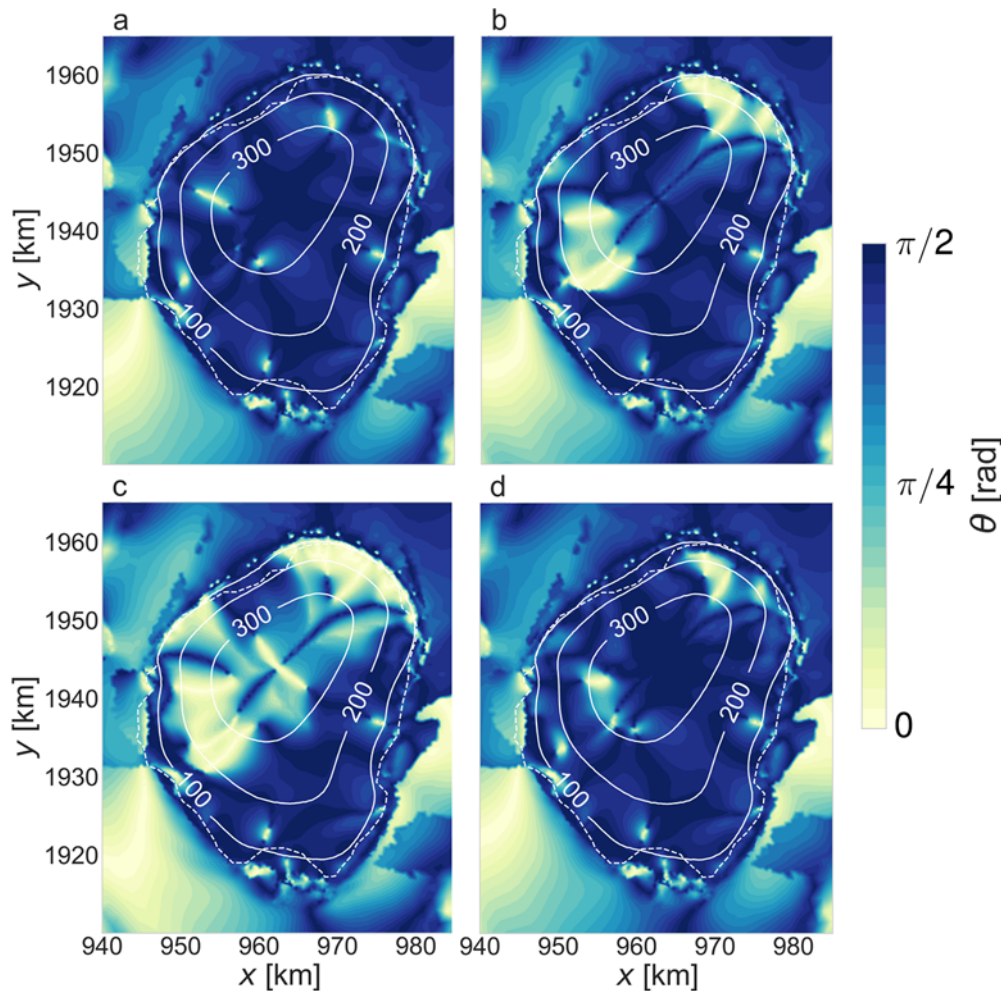


Figure 11. The angle between the eigenvectors corresponding to the larger horizontal crystal orientation eigenvalue and the larger horizontal strain rate eigenvalue for (a) the $\alpha = 0$, $\iota = 1$ simulation, (b) the $\alpha = 0$, $\iota = 0.6$ simulation, (c) the $\alpha = 1$, $\iota = 1$ simulation and (d) the $\alpha = 0.06$, $\iota = 1$ simulation.

single maximum will experience ease of deformation parallel to basal planes and stiffening in response to deformation parallel to the c -axes. In the simulations of DIR, a single maximum fabric is most apparent in the $\alpha = 0$, $\iota = 1$ and the $\alpha = 0.06$, $\iota = 1$ simulations (Fig. 4). If enhancement factors were used (Gillet-Chaulet and others, 2005; Ma and others, 2010) in a coupling with the ice viscosity, this would allow more ease of vertical shear in these areas which is important in the evolution of Raymond arches at flow divides, as shown in two-dimensional, anisotropic simulations (Martin and others, 2009; Martin and Gudmundsson, 2012; Drews and others, 2015).

A number of hurdles hinder the three-dimensional simulation of fully coupled ice anisotropy including computational expense, numerical instabilities, a lack of comparison with observations, parameter uncertainty and challenges associated with parallelisation. In a study by Gerber and others (2023) in which flow tube simulations of the Elmer/Ice model of fully coupled ice anisotropy were performed, it was noted that numerical instabilities significantly hindered the simulation of areas with high velocities. Furthermore, computational expense and an increased memory load means that a directional-dependent viscosity creates a further hindrance. Despite this, simulations such as those presented in this paper allow ease of comparison with observations and should

be included in comparisons between a hierarchy of models with varying complexity.

4.3. Model representation of anisotropy

Ice rises are an ideal location for testing models of ice anisotropy models as they contain various flow regimes which are relevant for other locations in the Antarctic Ice Sheet. Ice rises contain many of the same features as entire ice sheets, and results can inform expectations on studies in larger scales (Matsuoka and others, 2003). The shear zones on the western and eastern sides of DIR are representative of behaviour typical at lateral shear zones in ice shelves or ice streams (Smith and others, 2017). Similarly, flow divides, flank flow and ice shelf flow are typical in many areas of Antarctica. More studies are needed to examine whether an anisotropic flow law is needed in order to make accurate projections of sea level rise. This is especially important as sudden speed up of ice, for example, in the initiation of an ice stream, is associated with anisotropic behaviour (Thorsteinsson and others, 2003; Lilien and others, 2021; Gerber and others, 2023). This necessitates further studies for comparison between various hierarchies of isotropic and anisotropic ice flow models with varying model complexity as well as comparison with observations. In our approach, fabric anisotropy is

modelled using a crystal orientation tensor, which can describe many fabric types, but does not capture cone fabric shapes as modelled by Pettit and others (2007) or multiple single maxima. An example of a representation of crystal orientation which can capture complex fabrics has been developed by Rathmann and others (2021). Furthermore, the introduction of additional, higher-order crystal orientation tensors in Eq. (7) would allow a more accurate representation of crystal orientation distribution, yet would introduce additional computational expense.

In addition to difficulties in choosing a correct mathematical representation of an fabric anisotropy, Eq. (7) is challenging to solve numerically as it is an advection equation, with no diffusive term. We find that the use of semi-Lagrangian methods reduces dispersion, as they introduce diffusion through interpolation (Advani and Tucker, 1987). However, in areas with strong gradients in the velocity field, we nonetheless find that numerical dispersion deteriorates the solution with time. The alternative approach to this numerical problem has been to either explicitly incorporate numerical diffusion in Eq. (7) as in Seddik and others (2011) or to include re-crystallisation terms as in Gagliardini and others (2013). We find it to be more effective to constrain the degree of orientation, but our approach can easily be adapted to include a re-crystallisation term in Eq. (7).

4.4. Framework for comparison with observations

A crucial component of accurate modelling of the fabric anisotropy field of ice is the comparison with observations, which, until recently, have been possible only by comparison with a limited number of ice cores. From ice core data, it is possible to construct a crystal orientation tensor which is directly comparable to simulations such as those presented in this work. Recently, advances in the measurement of anisotropic fabric using radar have allowed the acquisition of a significant amount of data with much greater ease than expensive ice coring projects (Young and others, 2021a; 2021b; Ershadi and others, 2022; 2025). However, assumptions made in the processing of data mean that the methods currently used are only valid where the dominant *c*-axis direction is exactly vertical (Rathmann and others, 2022).

Thus far, observational fabric anisotropy data have been used for inferring ice flow history including flow re-organisation (Durand and others, 2007; Matsuoka and others, 2012; Brisbourne and others, 2019; 2021) as well as for investigation of the state of the ice fabric in ice conditions such as ice streams (Smith and others, 2017; Kufner and others, 2023), in layers of enhanced shear (Pettit and others, 2011) and at ice rises (Drews and others, 2015; Ershadi and others, 2025). In terms of making comparisons between observations and anisotropic models, matching of isochrones and velocities has been performed (Drews and others, 2015; McCormack and others, 2022), but few studies have compared directly the observed and modelled fabric anisotropy fields (Lilien and others, 2023).

Although we do not explicitly make comparisons between the observed and modelled fabric anisotropy fields of DIR, we have described steps necessary for such a comparison. Our results show very differing three-dimensional fabric anisotropy fields depending on the chosen influence of the strain rate and deviatoric stress tensors in Eq. (7) used in previous studies Martin and others (2009); Seddik and others (2011); Martin and Gudmundsson (2012); Gagliardini and others (2013) and draw attention to the need to constrain equation parameters. We have provided a method to compare the difference between the two horizontal eigenvalues (Fig. 10), sometimes referred to as the *horizontal*

anisotropy, which is directly comparable to radar observations. We recommend radar surveys in the areas of high horizontal flow divergence at the tails of flow divides, as these are areas where differing values of α and ι show significantly differing fabric anisotropy fields.

5. Conclusions

In this study, we have modelled the three-dimensional, diagnostic, fabric anisotropy field of DIR including domain partitioning using a crystal orientation tensor evolution equation describing the spatial distribution of ice crystal *c*-axes in a given ice volume. Simulations are performed varying the relative influence of the strain rate and deviatoric stress tensors in the crystal orientation tensor evolution equation as used in four previous studies (Martin and others, 2009; Seddik and others, 2011; Martin and Gudmundsson, 2012; Gagliardini and others, 2013), with results showing significantly differing ice fabrics across the flow divide and the flanks of DIR. Lastly, we provide a modelling framework for comparison with radar observations, outlining areas where the assumption of one vertical eigenvector may not hold and resulting errors in horizontal eigenvalues.

Data availability statement. The code needed to perform the simulations and create the presented in the figures here are available in a publicly accessible, permanent repository (Henry, 2024d). The accompanying model input and output data as well as the processed data are also available in a publicly accessible, permanent repository (Henry, 2024c). The simulations presented here are dependent on the results of simulations presented in a previous study (Henry and others, 2023), for which code and data are available (Henry, 2024a, b).

Acknowledgements. C.H. was supported by the Deutsche Forschungsgemeinschaft in the framework of the priority programme 1158 'Antarctic Research with comparative investigations in Arctic ice areas' by a grant SCHA 2139/1-1. R.D. was partially supported by an Emmy Noether Grant of the Deutsche Forschungsgemeinschaft (DR 822/3-1). This work used resources of the Deutsches Klimarechenzentrum granted by its Scientific Steering Committee. We would like to thank the reviewers and editor for comments which helped to improve the clarity of the text. We would furthermore like to thank Luca Schmidt for an internal review of the manuscript.

Author contribution. A.C.J.H. and C.M. designed the study, A.C.J.H. performed the simulations with input from C.M., A.C.J.H. performed the analysis with input from C.M. and A.C.J.H. wrote the manuscript which was edited by C.M. and R.D.

Competing interests. We have no competing interests to declare.

References

- Advani SG and Tucker ICL (1987) The use of tensors to describe and predict fiber orientation in short fiber composites. *Journal of Rheology* **31**, 751–784. doi: 10.1122/1.549945
- Alley RB (1988) Fabrics in polar ice sheets: development and prediction. *Science* **240**, 493–495. doi: 10.1126/science.240.4851.493
- Brisbourne AM, Kendall M, Kufner SK, Hudson TS and Smith AM (2021) Downhole distributed acoustic seismic profiling at Skytrain Ice Rise, West Antarctica. *The Cryosphere* **15**, 3443–3458. doi: 10.5194/tc-15-3443-2021
- Brisbourne AM, Martin C, Smith AM, Baird AF, Kendall JM and Kingslake J (2019) Constraining recent ice flow history at Korff Ice Rise, West Antarctica, using radar and seismic measurements of ice fabric. *Journal of Geophysical Research: Earth Surface* **124**, 175–194. doi: 10.1029/2018JF004776
- Callens D, Drews R, Witrant E, Philippe M and Pattyn F (2016) Temporally stable surface mass balance asymmetry across an ice rise derived from radar internal reflection horizons through inverse modeling. *Journal of Glaciology* **62**(233), 525–534. doi: 10.1017/jog.2016.41

- Castelnaud O, Duval P, Lebensohn RA and Canova GR** (1996) Viscoplastic modeling of texture development in polycrystalline ice with a self-consistent approach: Comparison with bound estimates. *Journal of Geophysical Research: Solid Earth* **101**, 13851–13868. doi: [10.1029/96JB00412](https://doi.org/10.1029/96JB00412)
- Chung DH and Kwon TH** (2002) Invariant-based optimal fitting closure approximation for the numerical prediction of flow-induced fiber orientation. *Journal of Rheology* **46**(1), 169–194. doi: [10.1122/1.1423312](https://doi.org/10.1122/1.1423312)
- Cintra JS and Tucker CL** (1995) Orthotropic closure approximations for flow-induced fiber orientation. *Journal of Rheology* **39**, 1095–1122. doi: [10.1122/1.550630](https://doi.org/10.1122/1.550630)
- Dall J** (2010) Ice sheet anisotropy measured with polarimetric ice sounding radar. In *2010 IEEE International Geoscience and Remote Sensing Symposium*, 2507–2510. doi: [10.1109/IGARSS.2010.5653528](https://doi.org/10.1109/IGARSS.2010.5653528)
- Diez A and 7 others** (2014) Influence of ice crystal anisotropy on seismic velocity analysis. *Annals of Glaciology* **55**, 97–106. doi: [10.3189/2014AoG67A002](https://doi.org/10.3189/2014AoG67A002)
- Drews R, Eisen O, Steinhage D, Weikusat I, Kipfstuhl S and Wilhelms F** (2012) Potential mechanisms for anisotropy in ice-penetrating radar data. *Journal of Glaciology* **58**(209), 613–624. doi: [10.3189/2012JoG11J114](https://doi.org/10.3189/2012JoG11J114)
- Drews R, Matsuoka K, Martin C, Callens D, Bergeot N and Pattyn F** (2015) Evolution of Derwael Ice Rise in Dronning Maud Land, Antarctica, over the last millennia. *Journal of Geophysical Research: Earth Surface* **120**, 564–579. doi: [10.1002/2014JF003246](https://doi.org/10.1002/2014JF003246)
- Durand G and 8 others** (2007) Change in ice rheology during climate variations—implications for ice flow modelling and dating of the epica dome c core. *Climate of the Past* **3**, 155–167. doi: [10.5194/cp-3-155-2007](https://doi.org/10.5194/cp-3-155-2007)
- Durand G, Gagliardini O, de Fleurian B, Zwinger T and Le Meur E** (2009) Marine ice sheet dynamics: Hysteresis and neutral equilibrium. *Journal of Geophysical Research* **114**, F03009. doi: [10.1029/2008JF001170](https://doi.org/10.1029/2008JF001170)
- Duval P, Ashby M and Anderman I** (1983) Rate-controlling processes in the creep of polycrystalline ice. *The Journal of Physical Chemistry* **87**, 4066–4074. doi: [10.1021/j100244a014](https://doi.org/10.1021/j100244a014)
- Ershadi MR and 9 others** (2022) Polarimetric radar reveals the spatial distribution of ice fabric at domes and divides in East Antarctica. *The Cryosphere* **16**, 1719–1739. doi: [10.5194/tc-16-1719-2022](https://doi.org/10.5194/tc-16-1719-2022)
- Ershadi MR and 10 others** (2025) Investigating the dynamic history of a promontory ice rise using radar data. *Journal of Glaciology* **71**, e1. doi: [10.1017/jog.2024.70](https://doi.org/10.1017/jog.2024.70)
- Favier L and Pattyn F** (2015) Antarctic ice rise formation, evolution, and stability. *Geophysical Research Letters* **42**, 4456–4463. doi: [10.1002/2015GL064195](https://doi.org/10.1002/2015GL064195)
- Fujita S, Maeno H and Matsuoka K** (2006) Radio-wave depolarization and scattering within ice sheets: a matrix-based model to link radar and ice-core measurements and its application. *Journal of Glaciology* **52**(178), 407–424. doi: [10.3189/172756506781828548](https://doi.org/10.3189/172756506781828548)
- Gagliardini O and 14 others** (2013) Capabilities and performance of Elmer/Ice, a new-generation ice sheet model. *Geoscientific Model Development* **6**, 1299–1318. doi: [10.5194/gmd-6-1299-2013](https://doi.org/10.5194/gmd-6-1299-2013)
- Gagliardini O, Gillet-Chaulet F and Montagnat M** (2009) A review of anisotropic polar ice models: from crystal to ice-sheet flow models. *Low Temperature Science* **68** (Supplement Issue “Physics of Ice Core Records II” (URL <https://hdl.handle.net/2115/45447>)), **68**, 149–166.
- Gagliardini O and Meyssonier J** (2002) Lateral boundary conditions for a local anisotropic ice-flow model. *Annals of Glaciology* **35**, 503–509. doi: [10.3189/172756402781817202](https://doi.org/10.3189/172756402781817202)
- Gerber TA and 11 others** (2023) Crystal orientation fabric anisotropy causes directional hardening of the Northeast Greenland Ice Stream. *Nature Communications* **14**, 2653. doi: [10.1038/s41467-023-38139-8](https://doi.org/10.1038/s41467-023-38139-8)
- Gillet-Chaulet F, Gagliardini O, Meyssonier J, Montagnat M, and Castelnaud O** (2005) A user-friendly anisotropic flow law for ice-sheet modeling. *Journal of Glaciology* **51**(172), 3–14. doi: [10.3189/172756505781829584](https://doi.org/10.3189/172756505781829584)
- Gillet-Chaulet F, Gagliardini O, Meyssonier J, Zwinger T, and Ruokolainen J** (2006) Flow-induced anisotropy in polar ice and related ice-sheet flow modelling. *Journal of Non-Newtonian Fluid Mechanics* **134**, 33–43. doi: [10.1016/j.jnnfm.2005.11.005](https://doi.org/10.1016/j.jnnfm.2005.11.005)
- Gödert G** (2003) A mesoscopic approach for modelling texture evolution of polar ice including recrystallization phenomena. *Annals of Glaciology* **37**, 23–28. doi: [10.3189/172756403781815375](https://doi.org/10.3189/172756403781815375)
- Henry ACJ** (2024a) Code for the publication “Predicting the three-dimensional stratigraphy of an ice rise” (Version v1). Zenodo. <https://doi.org/10.5281/zenodo.12180129>, (accessed 20 June 2024).
- Henry ACJ** (2024b) Data for the publication “Predicting the three-dimensional stratigraphy of an ice rise” (Version v1). Zenodo. <https://doi.org/10.5281/zenodo.12183293>, (accessed 20 June 2024).
- Henry ACJ** (2024c) Model input data, simulation output data and processed data presented in “modelling the three-dimensional, diagnostic anisotropy field of an ice rise” *Authorea* (Version v1). Zenodo. <https://doi.org/10.5281/zenodo.13143591>, (accessed 31 July 2024).
- Henry ACJ** (2024d) Simulation and post-processing code presented in “modelling the three-dimensional, diagnostic anisotropy field of an ice rise” (Version v1). Zenodo. <https://doi.org/10.5281/zenodo.13143326>, (accessed 31 July 2024).
- Henry ACJ, Drews R, Schannwell C and Višnjević V** (2022) Hysteretic evolution of ice rises and ice rumples in response to variations in sea level. *The Cryosphere* **16**, 3889–3905. doi: [10.5194/tc-16-3889-2022](https://doi.org/10.5194/tc-16-3889-2022)
- Henry ACJ, Schannwell C, Višnjević V, Millstein J, Bons P, Eisen O and R D** (2023) Predicting the three-dimensional age-depth field of an ice rise. doi: [10.22541/essoar.169230234.44865946/v1](https://doi.org/10.22541/essoar.169230234.44865946/v1)
- Jezek KC, Curlander JC, Carsey F, Wales C and Barry RG** (2013) RAMP AMM-1 SAR Image Mosaic of Antarctica, Version 2. doi: [10.5067/8AF4ZRPULS4H](https://doi.org/10.5067/8AF4ZRPULS4H)
- Jordan TM, Martín C, Brisbourne AM, Schroeder DM and Smith AM** (2022) Radar characterization of ice crystal orientation fabric and anisotropic viscosity within an Antarctic ice stream. *Journal of Geophysical Research: Earth Surface* **127**, e2022JF006673. doi: [10.1029/2022JF006673](https://doi.org/10.1029/2022JF006673)
- Koch I and 9 others** (2024) Radar internal reflection horizons from multi-system data reflect ice dynamic and surface accumulation history along the Princess Ragnhild Coast, Dronning Maud Land, East Antarctica. *Journal of Glaciology* **70**, e18. doi: [10.1017/jog.2023.93](https://doi.org/10.1017/jog.2023.93)
- Kufner S and 6 others** (2023) Strongly depth-dependent ice fabric in a fast-flowing Antarctic ice stream revealed with icequake observations. *Journal of Geophysical Research: Earth Surface* **128**, e2022JF006853. doi: [10.1029/2022JF006853](https://doi.org/10.1029/2022JF006853)
- Lilien DA and 6 others** (2023) Simulating higher-order fabric structure in a coupled, anisotropic ice-flow model: Application to Dome C. *Journal of Glaciology* **69**(278), 2007–2026. doi: [10.1017/jog.2023.78](https://doi.org/10.1017/jog.2023.78)
- Lilien DA, Rathmann NM, Hvidberg CS and Dahl-Jensen D** (2021) Modeling ice-crystal fabric as a proxy for ice-stream stability. *Journal of Geophysical Research: Earth Surface* **126**, e2021JF006306. doi: [10.1029/2021JF006306](https://doi.org/10.1029/2021JF006306)
- Llorens MG and 9 others** (2022) Can changes in deformation regimes be inferred from crystallographic preferred orientations in polar ice? *The Cryosphere* **16**, 2009–2024. doi: [10.5194/tc-16-2009-2022](https://doi.org/10.5194/tc-16-2009-2022)
- Ma Y, Gagliardini O, Ritz C, Gillet-Chaulet F, Durand G and Montagnat M** (2010) Enhancement factors for grounded ice and ice shelves inferred from an anisotropic ice-flow model. *Journal of Glaciology* **56**(199), 805–812. doi: [10.3189/002214310794457209](https://doi.org/10.3189/002214310794457209)
- Martín C and Gudmundsson GH** (2012) Effects of nonlinear rheology, temperature and anisotropy on the relationship between age and depth at ice divides. *The Cryosphere* **6**, 1221–1229. doi: [10.5194/tc-6-1221-2012](https://doi.org/10.5194/tc-6-1221-2012)
- Martín C, Hindmarsh RCA and Navarro FJ** (2009) On the effects of divide migration, along-ridge flow, and basal sliding on isochrones near an ice divide. *Journal of Geophysical Research* **114**, F02006. doi: [10.1029/2008JF001025](https://doi.org/10.1029/2008JF001025)
- Matsuoka K and 6 others** (2003) Crystal orientation fabrics within the Antarctic Ice Sheet revealed by a multipolarization plane and dual-frequency radar survey. *Journal of Geophysical Research: Solid Earth* **108**, 2003JB002425. doi: [10.1029/2003JB002425](https://doi.org/10.1029/2003JB002425)
- Matsuoka K and 19 others** (2015) Antarctic ice rises and rumples: Their properties and significance for ice-sheet dynamics and evolution. *Earth-Science Reviews* **150**, 724–745. doi: [10.1016/j.earscirev.2015.09.004](https://doi.org/10.1016/j.earscirev.2015.09.004)
- Matsuoka K, Power D, Fujita S and Raymond CF** (2012) Rapid development of anisotropic ice-crystal-alignment fabrics inferred from englacial radar polarimetry, central West Antarctica. *Journal of Geophysical Research: Earth Surface* **117**, F03029. doi: [10.1029/2012JF002440](https://doi.org/10.1029/2012JF002440)

- Matsuoka K, Wilen L, Hurley S and Raymond C** (2009) Effects of birefringence within ice sheets on obliquely propagating radio waves. *IEEE Transactions on Geoscience and Remote Sensing* **47**, 1429–1443. doi: [10.1109/TGRS.2008.2005201](https://doi.org/10.1109/TGRS.2008.2005201)
- McCormack FS, Warner RC, Seroussi H, Dow CF, Roberts JL and Treverrow A** (2022) Modeling the deformation regime of Thwaites Glacier, West Antarctica, using a simple flow relation for ice anisotropy (ESTAR). *Journal of Geophysical Research: Earth Surface* **127**, e2021JF006332. doi: [10.1029/2021JF006332](https://doi.org/10.1029/2021JF006332)
- Montagnat M and 9 others** (2014) Fabric along the NEEM ice core, Greenland, and its comparison with GRIP and NGRIP ice cores. *The Cryosphere* **8**, 1129–1138. doi: [10.5194/tc-8-1129-2014](https://doi.org/10.5194/tc-8-1129-2014)
- Pettit EC and 6 others** (2011) The crossover stress, anisotropy and the ice flow law at Siple Dome, West Antarctica. *Journal of Glaciology* **57**(201), 39–52. doi: [10.3189/002214311795306619](https://doi.org/10.3189/002214311795306619)
- Pettit EC, Thorsteinsson T, Jacobson HP and Waddington ED** (2007) The role of crystal fabric in flow near an ice divide. *Journal of Glaciology* **53**, 277–288. doi: [10.3189/172756507782202766](https://doi.org/10.3189/172756507782202766)
- Rathmann NM, Hvidberg CS, Grinsted A, Lilien DA and Dahl-Jensen D** (2021) Effect of an orientation-dependent non-linear grain fluidity on bulk directional enhancement factors. *Journal of Glaciology* **67**(263), 569–575. doi: [10.1017/jog.2020.117](https://doi.org/10.1017/jog.2020.117)
- Rathmann NM, Lilien DA, Grinsted A, Gerber TA, Young TJ and Dahl-Jensen D** (2022) On the limitations of using polarimetric radar sounding to infer the crystal orientation fabric of ice masses. *Geophysical Research Letters* **49**, e2021GL096244. doi: [10.1029/2021GL096244](https://doi.org/10.1029/2021GL096244)
- Richards DH, Pegler SS and Piazzolo S** (2022) Ice fabrics in two-dimensional flows: beyond pure and simple shear. *The Cryosphere* **16**, 4571–4592. doi: [10.5194/tc-16-4571-2022](https://doi.org/10.5194/tc-16-4571-2022)
- Richards DH, Pegler SS, Piazzolo S, Stoll N and Weikusat I** (2023) Bridging the gap between experimental and natural fabrics: Modeling ice stream fabric evolution and its comparison with ice-core data. *Journal of Geophysical Research: Solid Earth* **128**, e2023JB027245. doi: [10.1029/2023JB027245](https://doi.org/10.1029/2023JB027245)
- Rignot JM E and Scheuchl B** (2017) MEASURES InSAR-based Antarctica ice velocity map, version 2. doi: [10.5067/D7GK8F5J8M8R](https://doi.org/10.5067/D7GK8F5J8M8R)
- Schannwell C and 7 others** (2020) Quantifying the effect of ocean bed properties on ice sheet geometry over 40 000 years with a full-Stokes model. *The Cryosphere* **14**, 3917–3934. doi: [10.5194/tc-14-3917-2020](https://doi.org/10.5194/tc-14-3917-2020)
- Schannwell C, Drews R, Ehlers TA, Eisen O, Mayer C and Gillet-Chaulet F** (2019) Kinematic response of ice-rise divides to changes in ocean and atmosphere forcing. *The Cryosphere* **13**, 2673–2691. doi: [10.5194/tc-13-2673-2019](https://doi.org/10.5194/tc-13-2673-2019)
- Seddik H, Greve R, Zwinger T and Placidi L** (2011) A full Stokes ice flow model for the vicinity of Dome Fuji, Antarctica, with induced anisotropy and fabric evolution. *The Cryosphere* **5**, 495–508. doi: [10.5194/tc-5-495-2011](https://doi.org/10.5194/tc-5-495-2011)
- Smith EC and 6 others** (2017) Ice fabric in an Antarctic ice stream interpreted from seismic anisotropy. *Geophysical Research Letters* **44**, 3710–3718. doi: [10.1002/2016GL072093](https://doi.org/10.1002/2016GL072093)
- Thorsteinsson T, Waddington ED and Fletcher RC** (2003) Spatial and temporal scales of anisotropic effects in ice-sheet flow. *Annals of Glaciology* **37**, 40–48. doi: [10.3189/172756403781815429](https://doi.org/10.3189/172756403781815429)
- Weikusat I and 10 others** (2017) Physical analysis of an Antarctic ice core-towards an integration of micro- and macrodynamics of polar ice. *Philosophical Transactions of the Royal Society A: Mathematical, Physical and Engineering Sciences* **375**, 20150347. doi: [10.1098/rsta.2015.0347](https://doi.org/10.1098/rsta.2015.0347)
- Woodcock NH** (1977) Specification of fabric shapes using an eigenvalue method. *Geological Society of America Bulletin* **88**, 1231. doi: [10.1130/0016-7606\(1977\)88<1231:SOFSUA>2.0.CO;2](https://doi.org/10.1130/0016-7606(1977)88<1231:SOFSUA>2.0.CO;2)
- Young TJ and 6 others** (2021b) Inferring ice fabric from birefringence loss in airborne radargrams: Application to the eastern shear margin of Thwaites Glacier, West Antarctica. *Journal of Geophysical Research: Earth Surface* **126**, e2020JF006023. doi: [10.1029/2020JF006023](https://doi.org/10.1029/2020JF006023)
- Young TJ, Martín C, Christoffersen P, Schroeder DM, Tulaczyk SM and Dawson EJ** (2021a) Rapid and accurate polarimetric radar measurements of ice crystal fabric orientation at the Western Antarctic Ice Sheet (WAIS) Divide ice core site. *The Cryosphere* **15**, 4117–4133. doi: [10.5194/tc-15-4117-2021](https://doi.org/10.5194/tc-15-4117-2021)

Appendix

The representation of the fabric anisotropy field using a crystal orientation tensor,

$$\mathbf{a}^{(2)} = \begin{pmatrix} a_{xx}^{(2)} & a_{xy}^{(2)} & a_{xz}^{(2)} \\ a_{yx}^{(2)} & a_{yy}^{(2)} & a_{yz}^{(2)} \\ a_{zx}^{(2)} & a_{zy}^{(2)} & a_{zz}^{(2)} \end{pmatrix}, \quad (\text{A1})$$

describing the c -axis distribution is ideal for comparison with ice core or radar observations in that an equivalent crystal orientation tensor can be constructed from observational data by determining the cross-products of cosines of each c -axis and summing up such that

$$\mathbf{a}^{(2)} = \begin{pmatrix} a_{xx}^{(2)} & a_{xy}^{(2)} & a_{xz}^{(2)} \\ a_{yx}^{(2)} & a_{yy}^{(2)} & a_{yz}^{(2)} \\ a_{zx}^{(2)} & a_{zy}^{(2)} & a_{zz}^{(2)} \end{pmatrix} = \frac{1}{N} \begin{pmatrix} \sum l_i^2 & \sum l_i m_i & \sum l_i n_i \\ \sum m_i l_i & \sum m_i^2 & \sum m_i n_i \\ \sum n_i l_i & \sum n_i m_i & \sum n_i^2 \end{pmatrix}, \quad (\text{A2})$$

where N is the number of c -axes being summed over. The cosines of the c -axis vectors are defined by taking the cosine of the angle between the c -axis vector, \mathbf{c}_i , and each positive coordinate axis, $\hat{\mathbf{e}}_x$, $\hat{\mathbf{e}}_y$ and $\hat{\mathbf{e}}_z$, so that

$$\begin{aligned} l_i &= c_{i,x}, \\ m_i &= c_{i,y}, \\ n_i &= c_{i,z}. \end{aligned} \quad (\text{A3})$$

From the orientation tensor, a number of metrics can be calculated to investigate the degree of crystal orientation, the predominant c -axes directions and the fabric type.